CHAPTER 2

Cholesterol based mesogenic Schiff's base derivatives

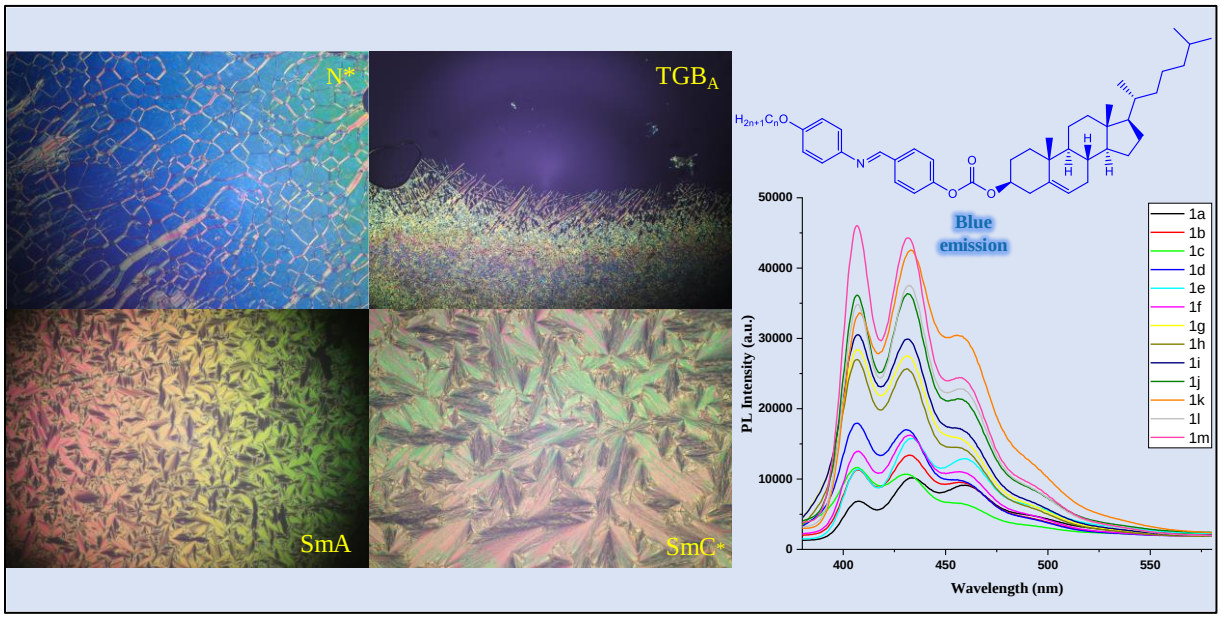

2.1. Introduction

Mesogens made of cholesterol are the first liquid crystals that have ever been discovered. Since they were the first species discovered more than a century ago and because their derivatives are probably the most studied mesogens, they continue to hold promise for fresh research in a variety of fields, from the development of electronic devices to optical technology [1,2]. LC based on cholesterol have gained considerable focus from scholars not only due to their natural and commercial availability but also because the helical supramolecular structure of cholesterol-based liquid crystals imparts some unique optical properties, such as selective reflection of circularly polarised light, high optical rotatory power, circular dichroism, and electro-optic effect [3]. Additionally, because these characteristics vary with variables like temperature, pressure, and electric field, they might find use in optical storage, colour display technology, and full-colour rewritable recording systems [4–6].

The synthesis of different cholesteryl esters, ethers, carbonates, carbamates, etc. is made possible by the C_3-hydroxyl group of cholesterol. These substances are frequently used in pharmaceuticals, the chemical industry, and toiletries and cosmetics [7].Such molecules have a propensity to aggregate into sizable three-dimensional structures in which the location and orientation of the molecule are organised due to both the stiff steroid backbone and its hydrophobic nature [8,9]. Also, cholesterol-based compounds have a wide range of uses ranging from drug delivery [10–13] or bioimaging applications [14–16] to cholesterol-based liquid crystals [17–19] and gelators [20,21], anticancer [22,23], antimicrobial [24–26] and antioxidant [27] applications; as well as purely synthetic applications [28,29].

Cholesterol has been widely used in chiral liquid crystalline materials due to its rigid structure with eight chiral centres and the simplicity with which the structure can be derivatized. They have the ability to generate a broad range of liquid crystalline phases, including frustrated phases, due to their intrinsic chirality, depending on the structure of the steroidal skeleton and the substituents attached [2,30]. The frustration of the phases is generally observed only in chiral systems with high enantiomeric excess and strong molecular chirality (short pitch). Despite the fact that many conventional (over 3000) monomeric liquid crystals consisting of cholesteryl ester unit as a chiral part of the molecule have been reported, there are only a few cholesterol-based mesogens exhibiting the TGB_A or related phases [31–34]. Many researchers have created thousands of monomers, oligomers, and polymers based on cholesterol due to the substance's capacity to induce a liquid crystalline characteristic in its many derivatives [35].

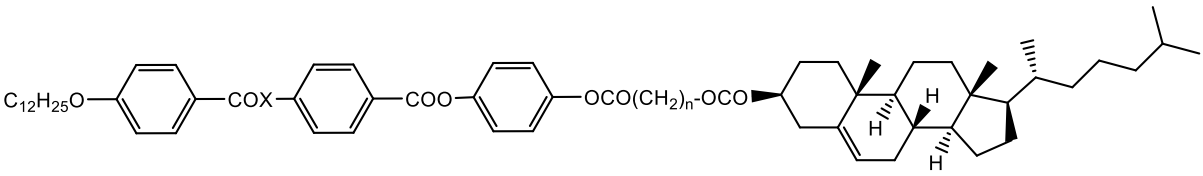

X=S n=2-8
X=O n=4

(a)

Figure 2.1 (a): Molecular structure of non-symmetric cholesterol-based liquid crystals with thioester linkages

Zhiming et al. [36] reported non-symmetric cholesterol-based twin liquid crystals with thioester linkages **Figure 2.1 (a)** exhibiting enantiotropic mesophase behaviour with an SmC* phase (broken focal conic texture) and a typical N* (cholesteric) phase (oily streaks texture) with significant odd-even effects clearing points (Ti) and entropy changes.

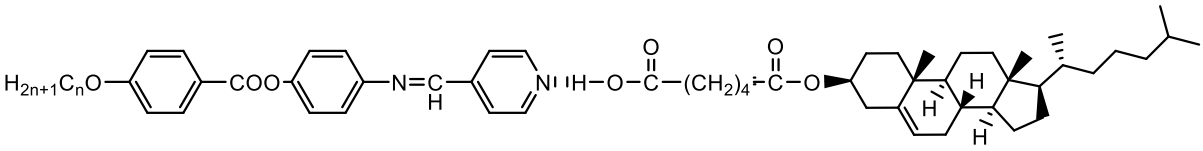

n= 4-8 & 10

(b)

Figure 2.1 (b): Molecular structure of cholesterol-based hydrogen-bonded liquid crystals

Jun-Woo Lee [37] reported cholesterol-based hydrogen-bonded liquid crystals **Figure 2.1 (b)**, which all exhibit a cholesteric mesophase. For n = 4–8, a SmA phase is seen after additional cooling. Prior to crystallisation, the chiral smectic C (SmC*) phase for n = 8 exists. The decyloxy homologue only exhibits a cholesteric – SmC* sequence.

Guan-Yeow Yeap et al. [38] synthesised non-symmetric liquid crystal dimers containing cholesterol, triazole and biphenylene with different flexible spacers **Figure 2.1 (c)** and concluded that although conjugates with shorter spacers (n = 5 and 6) exhibit enantiotropic SmA* and monotropic SmC* phases, those with longer spacers (n = 10) favour the production of enantiotropic SmA and N* phases. Additionally, it was found that the transition temperatures increased in direct proportion to the length of the methylene spacer, and that the even spacers had a greater clearing point. Using either odd-parity or even-parity spacers, Hiremath [39] reported the synthesis of two new series of cholesterol-biphen-4-yl 4-(n-alkoxy) benzoate conjugates in 2014 **Figure 2.1 (d)**.

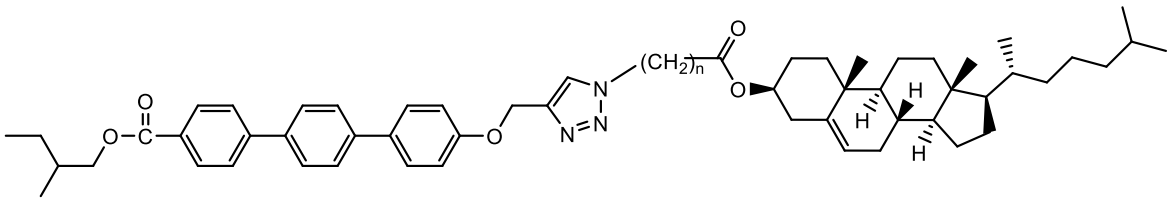

n= 5-10

(c)

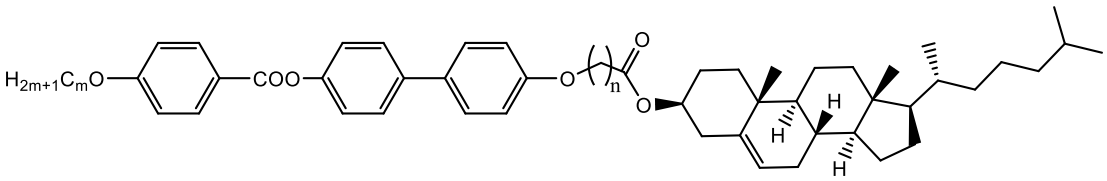

n=4 & 5 and
m=8-12 & 16

(d)

Figure 2.1 (c and **d):** Molecular structure of non-symmetric liquid crystal dimers

All the compounds are optically active, and both series of conjugates exhibit a frustrated liquid crystalline form with a thermodynamically stable twist grain boundary phase and chiral smectic C structure (TGB_C*) over a very broad temperature range.

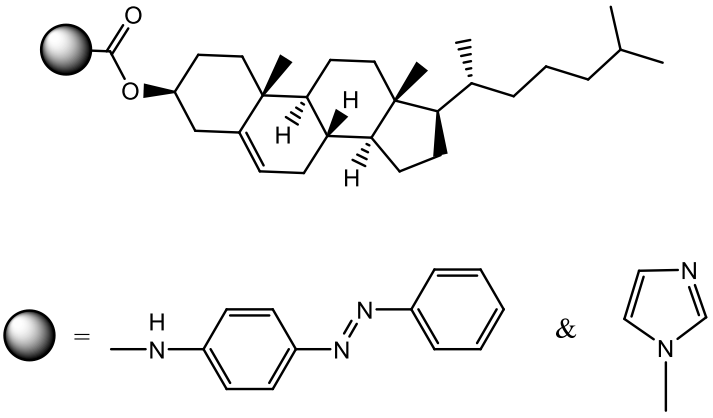

(e)

Figure 2.1 (e): Molecular structure of cholesteryl carbamate-based liquid crystals

Burak Korkmaz et al. [39] reported cholesteryl carbamate-based liquid crystals **Figure 2.1 (e)**. Both of the new compounds showed long-lasting enantiotropic polymorphism over a wide range of temperatures because of their carbamate functions.

Many other cholesterol-based monomers and dimers have been reported, exhibiting chiral nematic, Smectic A, smectic C*, and twist grain boundary mesophases [36,37,40–42]. Similarly, cholesterol-derived trimers and polymers also display these mesophases along with twist grain boundaries [38,43–46].

We hereby report the synthesis, characterisation, mesomorphic, and thermal studies of newly synthesised cholesteryl carbonate-based liquid crystal with Schiff's base linkage and terminal alkoxy chains.

2.2. Experimental Details

2.2.1. Materials

Cholesteryl chloroformate was purchased from Sigma-Aldrich Chemicals, USA. 4-Hydroxy benzaldehyde, paracetamol, alkyl bromides were purchased from Loba Chemie Pvt. Ltd. Tetrahydrofuran (THF), acetone and ethanol underwent drying treatment with standard methods. All other solvents and reagents were AR grade and used without further purification.

2.2.2. Techniques and Measurements

The compounds' structures were established utilizing conventional spectroscopic techniques. Thin-layer chromatography (TLC) was performed on silica gel plates (Merck). FT-IR spectra were recorded on a Bruker spectrometer as KBr Pellets. ^{1}H NMR and ^{13}C NMR spectral data were recorded on an Avance Bruker 400 spectrometer (400 MHz) with Deuterated Chloroform ($CDCl_3$) as solvent and TMS as Internal Standard. The polarised optical microscopy (POM) study was observed with a Nikon Eclipse C*i*-Pol microscope equipped with a Linkam (Linkam, Surrey, England) heating stage. Phase transition temperatures and thermodynamic parameters were determined by using differential scanning calorimetry (DSC-822, Mettler Toledo, having Stare software). The heating and cooling rates were set at 10°C/min. Calibration of the instrument was performed using indium as a standard. The thermal stability of the compounds was recorded using a Thermogravimetry Analyzer (TGA-50, Shimadzu, Japan) with 3-7 mg of the sample in platinum pan at a heating rate of 10°C/min. Thermo Finnigan's (Flash 1112 series EA) CHN analyzer was used to carry out elemental analyses. Absorbance was recorded using a Shimadzu UV-1800 spectrophotometer (Japan). Photoluminescence and quantum yields (Φ_{PL}) were measured using a Shimadzu RF 6000 Spectro fluorophotometer (Japan). Gaussian 09, revision A.02 software was utilized for DFT calculations.

2.2.3. Synthesis and characterisation

The synthetic routes of the mesogenic Schiff's base are shown in **Scheme 2.1**.

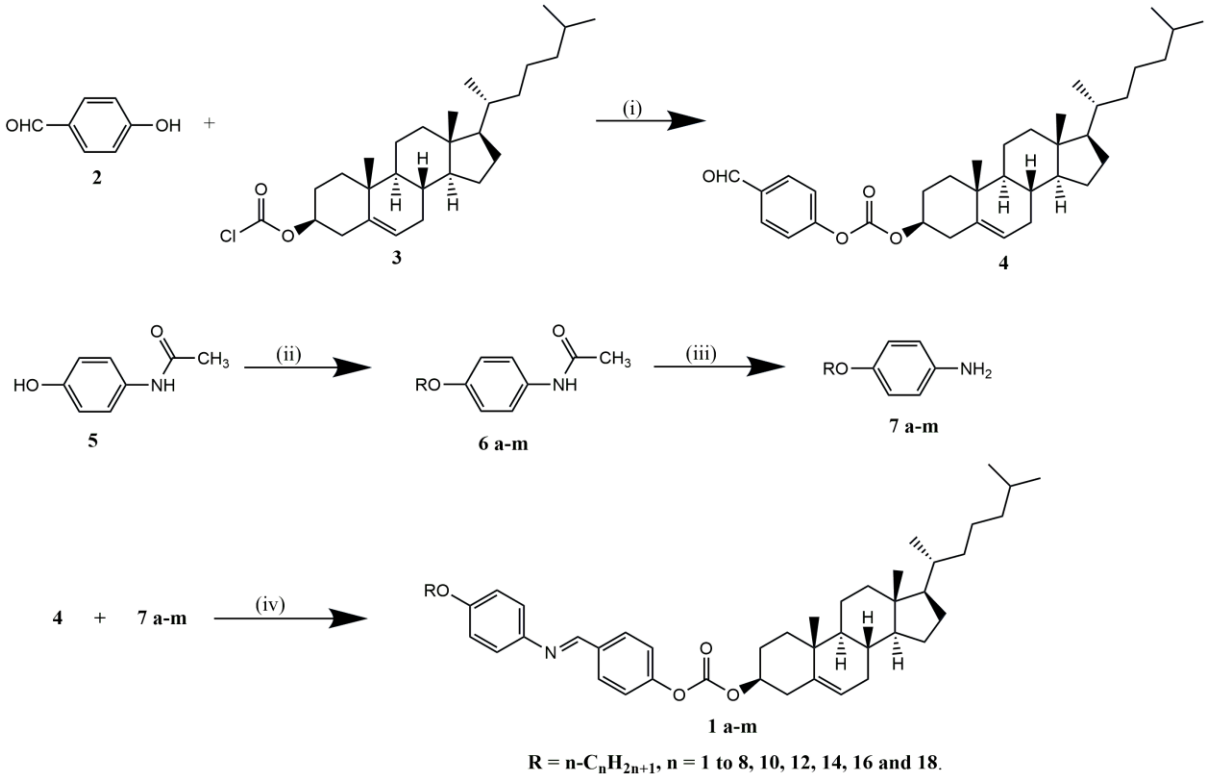

Scheme 2.1: Synthetic route to 1 a-m. (i) Dry THF, pyridine, stirring 3-4 h at 38-40°C, (ii) n-alkyl bromide, dry acetone, anhydrous K_2CO_3, reflux for 8-10 h, (iii) 50% hydrochloric acid, 90-95°C, 10-12 h, (iv) chloroform: methanol (1:1), glacial acetic acid, 3-4 h.

*2.2.3.1. Synthesis of 4-formyl phenyl cholesteryl carbonate **(4)***

In a round-bottom flask, cholesteryl chloroformate (0.01 mol) **(3)** and dry THF (50 ml) were taken. To the reaction mixture, 4-hydroxy benzaldehyde (0.011 mol) **(2)**, anhydrous pyridine (4.0 ml), and an additional dry THF (40 ml) were added. After stirring for 2-3 h at 38-40°C, the mixture was filtered to isolate pyridinium chloride salt and other solids. The filtrate was concentrated under vacuum to remove excess THF, and n-hexane was added. After filtration, the resulting precipitates were crystallized from an ethyl acetate-methanol mixture (70:30) until a consistent transition temperature was obtained. This compound **(4)** was found to be mesogenic in nature.

Compound 4: White crystalline solid, yield 65%, phase transition: Cr 139.0°C N* 188.9°C Iso171.8°C N* 116°C Cr, IR (KBr, ν_{max}, cm^{-1}): 2943, 2888, 2868, 2851, 2790, 2720, 1755, 1703, 1502, 839; ^{1}H-NMR ($CDCl_3$, 400 MHz): δ (ppm) = 9.91 (s, 1H, CHO), 7.92-7.94 (d, 2H, J = 8.8 Hz, Ar-H), 7.30-7.32 (d, 2H, J = 8.8 Hz, Ar-H), 5.44-5.46 (m, 1H, -C=CH-), 4.58-4.66 (m, 1H, -OCH-CH_2), 2.52 (q, 2H, -OCH-CH_2), 0.70-2.05 (m, 41H, -CH, -CH_2 and -CH_3); ^{13}C NMR ($CDCl_3$, 400MHz): δ(ppm) = 191.2 (CHO), 158.36, 150.1 (-O-COO-), 158.36, 139.08, 134.19, 129.75, 122.22, 121.44, 79.13, 56.69, 56.13, 49.98, 42.33, 39.71, 39.53, 37.94, 36.84, 36.57, 36.19, 35.81, 31.92, 31.84, 28.24, 28.04, 27.65, 24.30, 23.84, 22.85, 22.58, 21.06, 19.31, 18.73, 11.84. Elemental analysis: calculated for $C_{35}H_{50}O_4$(%): C, 78.61; H, 9.42; found: C, 78.58, H; 9.46.

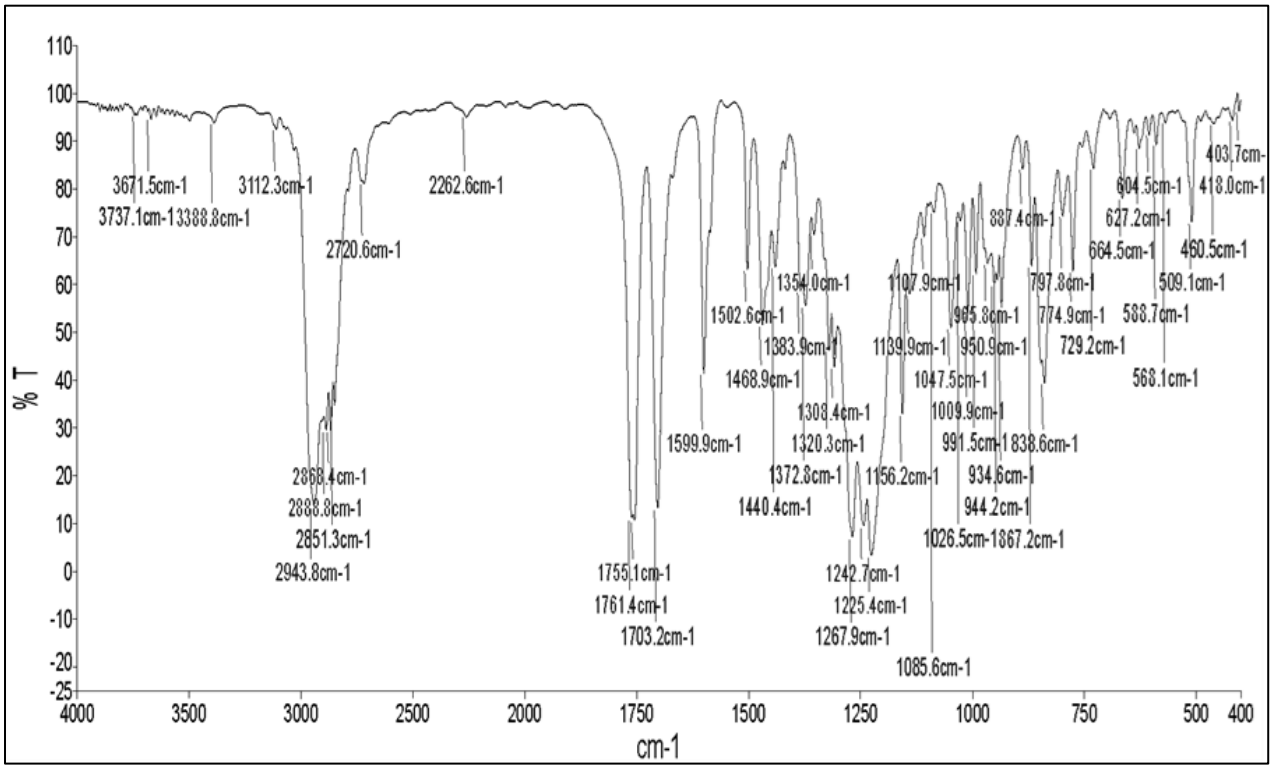

Figure 2.2 (a): FT-IR spectra of **Compound 4**

*2.2.3.2. Synthesis of 4-n-alkoxy acetanilide **(6 a-m)***

In a 100 ml three necked round-bottom flask, paracetamol (0.1 mol) **(5)**, anhydrous potassium carbonate (0.15 mol) and dry acetone (60 ml) were taken. The reaction mix was heated to 70-80°C with stirring. To the warm solution appropriate alkyl bromide (0.15 mol) was slowly added in 1 h. Mixture was then refluxed with continuous stirring at 70-80°C for 8 h. Then, it was cooled down to 25-30 °C and diluted using cold water. The solid mass was collected by filtration, washed with water and directly used for hydrolysis [47]. Yield: 80-90%.

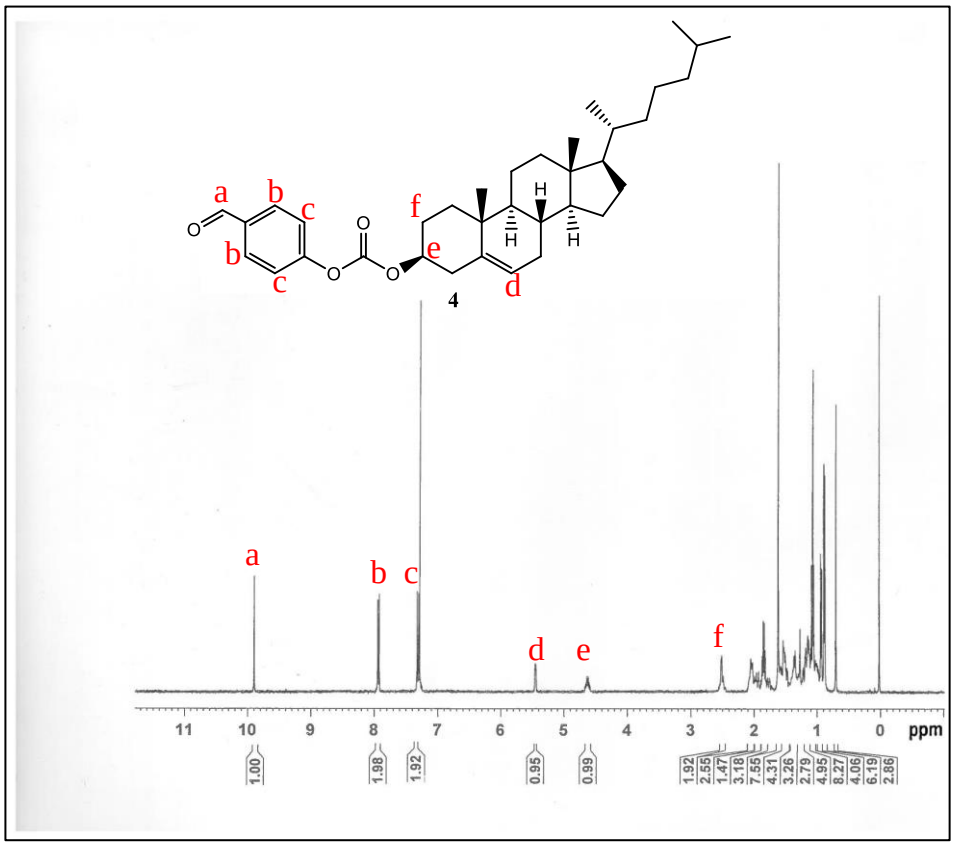

Figure 2.2 (b): ^{1}H-NMR spectra of **Compound 4**

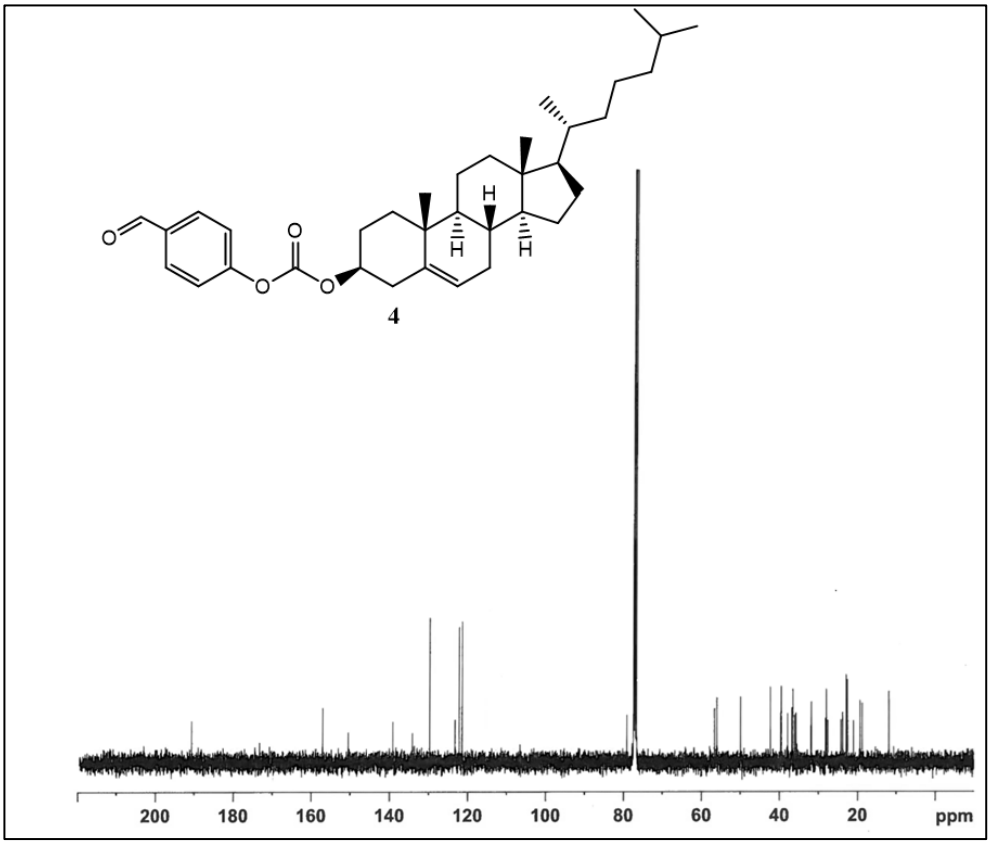

Figure 2.2 (c): ^{13}C-NMR spectra of **Compound 4**

*2.2.3.3. Synthesis of 4-n-alkoxy aniline **(7 a-m)***

A mixture of 4-n-alkoxy acetanilide (0.014 mol) (6 a-m), water (7 ml) and concentrated hydrochloric acid (4.5 ml) was stirred for 10 to 12 h at 90-95°C and then cooled to room temperature. The mixture was made alkaline with 50% sodium hydroxide solution at 20°C. The oily/waxy product was extracted with diethyl ether. After evaporation of solvent on a rotary evaporator the corresponding products were obtained as pale-yellow oils and higher member were obtained as light brown solids. Boiling/melting point agrees with the reported value [47]. Yield: 75-80%

*2.2.3.4. Synthesis of 4,4'-n-alkoxy benzylidene amino cholesteryl carbonate **(1 a-m)** [Final Schiff's base derivatives]*

A mixture of cholesterol derivative **(4)** (0.002 mol) and compounds **(7 a-m)** (0.004 mol) was refluxed in $CHCl_3$/MeOH (v: v=1:1) (20 ml) for 8 h. 2-3 drops of glacial acetic acid was added as catalyst. Progress of the reaction was measured using TLC which indicated disappearance of starting materials. Reaction mixture was kept overnight which gave pale yellow greenish needle shaped crystals. The product was filtered and recrystallized from chloroform: methanol (1:2) till relentless transition temperatures attained, giving pale yellow crystalline solid.

Compound 1a: Pale yellow crystalline solid, yield: 88.7%, IR (KBr, ν_{max}, cm^{-1}): 3034, 2944, 2897, 2867, 2847, 1753, 1623, 1506, 839; ^{1}H-NMR ($CDCl_3$, 400 MHz): δ(ppm) = 8.48 (s, 1H, CH=N), 7.92-7.94 (d, 2H, J = 8.8 Hz, Ar-H), 7.30-7.32 (d, 2H, J = 8.8 Hz, Ar-H), 7.24-7.26 (d, 2H, J = 8.8 Hz, Ar-H), 6.94-6.96 (d, 2H, J = 8.8 Hz, Ar-H), 5.44-5.45 (m, 1H, -C=CH-), 4.58-4.66 (m, 1H, -OC<u>H</u>-$CH_{2)}$, 3.86 (s, 3H, -OCH_3), 2.50-2.52 (q, 2H, -OCH-C<u>H</u>$_{2)}$, 0.70-2.05 (m, 41H, -CH, -CH_2 and -CH_3); ^{13}C NMR ($CDCl_3$, 400MHz): δ(ppm) = 158.36 (CH=N), 157.01, 153.07, 152.56 (-O-COO-), 144.69, 139.08, 134.19, 129.75, 123.30, 122.22, 121.44, 114.40, 79.13, 56.69, 56.13, 55.52, 49.94, 42.34, 39.72, 39.52, 37.94, 36.85, 36.57, 36.20, 35.81, 31.92, 31.85, 28.24, 28.02, 27.65, 24.32, 23.84, 22.86, 22.58, 21.07, 19.31, 18.73, 11.88; Elemental analysis: calculated for $C_{42}H_{57}NO_4$(%): C, 78.83; H, 8.98; N, 2.19; found: C, 78.65, H; 9.29; N; 2.02.

Compound 1b: Pale yellow crystalline solid, yield: 84.2%, IR (KBr, ν_{max}, cm^{-1}): 3045, 2949, 2868, 1757, 1626, 1508, 842; ^{1}H-NMR ($CDCl_3$, 400 MHz): δ(ppm) = 8.48 (s, 1H, CH=N), 7.92-7.94 (d, 2H, J = 8.4 Hz, Ar-H), 7.30-7.32 (d, 2H, J = 8.8 Hz, Ar-H), 7.23-7.25 (d, 2H, J = 8.8 Hz, Ar-H), 6.94-6.96 (d, 2H, J = 8.8 Hz, Ar-H), 5.44-5.45 (m, 1H, -C=CH-),

4.58-4.66 (m, 1H, -OCH-CH_2), 4.05-4.11(q, 2H, -CH_2-O-Ar), 2.50-2.52 (q, 2H, -OCH-CH_2), 0.70-2.05 (m, 44H, -CH, -CH_2 and -CH_3); ^{13}C NMR ($CDCl_3$, 400MHz): δ(ppm) = 159.4 (CH=N), 154.4, 152.58 (-O-COO-), 143.6, 139.0, 134.17, 129.7, 123.30, 122.22, 121.6, 115.7, 79.12, 64.6, 56.70, 56.12, 49.94, 42.37, 39.70, 39.51, 37.94, 36.85, 36.57, 36.21, 35.80, 31.92, 31.88, 28.24, 28.0, 27.65, 24.29, 23.84, 22.86, 22.58, 21.07, 19.31, 18.73,13.8, 11.88; Elemental analysis: calculated for $C_{43}H_{59}NO_4$(%): C, 78.98; H, 9.09; N, 2.14; found: C, 78.82, H; 8.99,N; 1.98.

Compound 1c: Pale yellow crystalline solid, yield: 86.4%, IR (KBr, ν_{max}, cm^{-1}): 3032, 2945, 2901, 2866, 1759, 1627, 1506, 838; ^{1}H-NMR ($CDCl_3$, 400 MHz): δ(ppm) = 8.48 (s, 1H, CH=N), 7.92-7.94 (d, 2H, J = 8.8 Hz, Ar-H), 7.30-7.32 (d, 2H, J = 8.8 Hz, Ar-H), 7.23-7.25 (d, 2H, J = 8.8 Hz, Ar-H), 6.93-6.96 (d, 2H, J = 8.8 Hz, Ar-H), 5.44-5.45 (m, 1H, -C=CH-), 4.58-4.66(m, 1H, -OCH-CH_2), 3.94-3.98 (t, 2H, -CH_2-O-Ar), 2.50-2.52 (q, 2H, -OCH-CH_2), 0.70-2.05 (m, 46H, -CH, -CH_2 and -CH_3); ^{13}C NMR ($CDCl_3$, 400MHz): δ(ppm) = 158.39 (CH=N), 157.9, 153.08, 152.54 (-O-COO-), 143.6, 139.06, 134.19, 129.7, 123.30, 122.21, 121.7, 115.7, 79.10, 69.3, 56.70, 56.11, 49.94, 42.34, 39.72, 39.51, 37.94, 36.85, 36.57, 36.21, 35.82, 31.92, 31.82, 28.24, 28.03, 27.65, 24.29, 23.84, 22.86, 22.58, 21.07, 19.31, 18.73, 11.88,10.4; Elemental analysis: calculated for $C_{44}H_{61}NO_4$(%): C, 79.12; H, 9.21; N, 2.10; found: C, 79.01, H; 9.07,N; 2.00.

Compound 1d: Pale yellow crystalline solid, yield: 87.8%, IR (KBr, ν_{max},cm^{-1}): 3030, 2934, 2862, 1759, 1625, 1506, 838; ^{1}H-NMR ($CDCl_3$, 400 MHz): δ(ppm) = 8.48 (s, 1H, CH=N), 7.92-7.94 (d, 2H, J = 8.4 Hz, Ar-H), 7.30-7.32 (d, 2H, J = 8.8 Hz, Ar-H), 7.23-7.25 (d, 2H, J = 8.8 Hz, Ar-H), 6.93-6.95 (d, 2H, J = 8.8 Hz, Ar-H), 5.44-5.45 (m, 1H, -C=CH-), 4.58-4.63 (m, 1H, -OCH-CH_2), 3.98-4.02 (t, 2H, -CH_2-O-Ar), 2.50-2.51 (q, 2H, -OCH-CH_2), 0.70-2.05 (m, 48H, -CH, -CH_2 and -CH_3); ^{13}C NMR ($CDCl_3$,400MHz): δ(ppm) = 157.98 (CH=N), 156.82, 153.07, 152.57 (-O-COO-), 144.47, 139.08, 134.24, 129.72, 123.30, 122.19, 121.43, 114.99, 79.12, 68.4, 56.69, 56.13, 49.98, 42.33, 39.71, 39.53, 37.94, 36.84, 36.57, 36.19, 35.81, 31.93, 31.85, 28.23, 28.04, 27.65, 24.30, 23.84, 22.85, 22.58,22.50, 21.06, 19.31, 18.98, 14.14, 11.88; Elemental analysis: calculated for $C_{45}H_{63}NO_4$(%): C, 79.25; H, 9.31; N, 2.05; found: C, 79.08, H; 9.13,N; 1.86.

Compound 1e: Pale yellow crystalline solid, yield: 84.2%, IR (KBr, ν_{max} , cm^{-1}): 3044, 2946, 2901, 2866, 1759, 1624, 1506, 838; ^{1}H-NMR ($CDCl_3$, 400 MHz): δ(ppm) = 8.48 (s, 1H, CH=N), 7.92-7.94 (d, 2H, J = 8.4 Hz, Ar-H), 7.30-7.32 (d, 2H, J = 8.4Hz, Ar-H), 7.23-7.25 (d, 2H, J = 8.8 Hz, Ar-H), 6.93-6.95 (d, 2H, J = 9.2 Hz, Ar-H), 5.44-5.45 (m, 1H, -C=CH-), 4.58-

4.66 (m, 1H, -OCH-CH_2), 3.09-4.01 (t, 2H, -CH_2-O-Ar), 2.50-2.52 (q, 2H, -OCH-CH_2), 0.70-2.05 (m, 50H, -CH, -CH_2 and -CH_3); ^{13}C NMR ($CDCl_3$,400MHz): δ(ppm) = 157.98 (CH=N), 156.82, 153.04, 152.57 (-O-COO-), 144.47, 139.08, 134.24, 129.72, 123.30, 122.19, 121.43, 114.99, 79.12, 68.29, 56.69, 56.13, 49.98, 42.33, 39.71, 39.53, 37.94, 36.84, 36.57, 36.19, 35.81, 31.93, 31.85,29.01, 28.23, 28.04, 27.65, 24.30, 23.84, 22.85, 22.58,22.50, 21.06, 19.31, 18.73, 14.14, 11.88; Elemental analysis: calculated for $C_{46}H_{65}NO_4$(%): C, 79.38; H, 9.41; N, 2.01; found: C, 79.15, H; 9.19,N; 1.89.

Compound 1f: Pale yellow crystalline solid, yield: 88.2%, IR (KBr, ν_{max}, cm^{-1}): 3036, 2953, 2868, 1757, 1624, 1508, 842; ^{1}H-NMR ($CDCl_3$, 400 MHz): δ(ppm) = 8.48 (s, 1H, CH=N), 7.92-7.94 (d, 2H, J = 8.4 Hz, Ar-H), 7.30-7.32 (d, 2H, J = 8.8Hz, Ar-H), 7.23-7.25 (d, 2H, J = 8.8 Hz, Ar-H), 6.93-6.95 (d, 2H, J = 8.8 Hz, Ar-H), 5.44-5.45 (m, 1H, -C=CH-), 4.58-4.64 (m, 1H, -OCH-CH_2), 3.98-4.00 (t, 2H, -CH_2-O-Ar), 2.49-2.51 (q, 2H, -OCH-CH_2), 0.70-2.05 (m, 52H, -CH, -CH_2 and -CH_3); ^{13}C NMR ($CDCl_3$,400MHz): δ(ppm) = 157.98 (CH=N), 156.82, 153.04, 152.58 (-O-COO-), 144.47, 139.08, 134.24, 129.72, 123.30, 122.19, 121.43, 114.99, 79.12, 68.27, 56.69, 56.13, 49.98, 42.33, 39.71, 39.53, 37.94, 36.84, 36.57, 36.19, 35.81, 31.93, 31.85, 29.30, 29.01, 28.28, 28.04, 27.65, 24.30, 23.84, 22.85, 22.58,22.50, 21.06, 19.35, 18.74, 14.14, 11.88; Elemental analysis: calculated for $C_{47}H_{67}NO_4$(%): C, 79.50; H, 9.51; N, 1.97; found: C, 79.36, H; 9.29,N; 1.72.

Compound 1g: Pale yellow crystalline solid, yield: 78.8%, IR (KBr, ν_{max}, cm^{-1}): 3041, 2949, 2860, 1764,1624, 1506, 838; ^{1}H-NMR ($CDCl_3$, 400 MHz): δ(ppm) = 8.48 (s, 1H, CH=N), 7.92-7.94 (d, 2H, J = 8.4 Hz, Ar-H), 7.30-7.32 (d, 2H, J = 8.8 Hz, Ar-H), 7.23-7.25 (d, 2H, J = 8.8 Hz, Ar-H), 6.93-6.95 (d, 2H, J = 8.8 Hz, Ar-H), 5.44-5.45 (m, 1H, -C=CH-), 4.58-4.66 (m, 1H, -OCH-CH_2), 3.97-4.01(t, 2H, -CH_2-O-Ar), 2.50-2.52 (q, 2H, -OCH-CH_2), 0.70-2.05 (m, 54H, -CH, -CH_2 and -CH_3); δ(ppm) = 157.99(CH=N), 156.81, 153.04, 152.57 (-O-COO-), 144.46, 139.08, 134.24, 129.72, 123.30, 122.19, 121.43, 114.99, 79.12, 68.30, 56.69, 56.13, 49.98, 42.33, 39.71, 39.53, 37.94, 36.84, 36.57, 36.19, 35.81, 31.93, 31.85, 31.81, 29.33, 29.10, 28.25, 28.04, 27.65, 24.30, 23.84, 22.85, 22.58,22.64, 22.59, 21.07, 19.35, 18.74, 14.14, 11.87; Elemental analysis: calculated for $C_{48}H_{69}NO_4$(%): C, 79.62; H, 9.61; N, 1.93; found: C, 79.46, H; 9.40,N; 1.72.

Compound 1h: Pale yellow crystalline solid, yield: 75.9%, IR (KBr, ν_{max}, cm^{-1}): 3034, 2938, 2855, 1758, 1626, 1505, 838; ^{1}H-NMR ($CDCl_3$, 400 MHz): δ(ppm) = 8.48 (s, 1H, CH=N), 7.92-7.94 (d, 2H, J = 8.4 Hz, Ar-H), 7.30-7.32 (d, 2H, J = 8.8 Hz, Ar-H), 7.23-7.25 (d, 2H, J = 8.8Hz, Ar-H), 6.93-6.95 (d, 2H, J = 8.8 Hz, Ar-H), 5.44-5.45 (m, 1H, -C=CH-),

4.59-4.63 (m, 1H, -OCH-CH_2), 3.97-3.99 (t, 2H, -CH_2-O-Ar), 2.50-2.52 (q, 2H, -OCH-CH_2), 0.70-2.05 (m, 56H, -CH, -CH_2 and -CH_3); ^{13}C NMR ($CDCl_3$,400MHz): δ(ppm) = 157.99 (CH=N), 156.81, 153.04, 152.57 (-O-COO-), 144.46, 139.08, 134.24, 129.72, 123.30, 122.19, 121.43, 114.99, 79.12, 68.30, 56.69, 56.13, 49.98, 42.33, 39.71, 39.53, 37.94, 36.84, 36.57, 36.19, 35.81, 31.93, 31.85, 31.81, 29.33, 29.10, 28.25, 28.04, 27.65, 24.30, 23.84, 22.85, 22.64, 22.59, 21.07, 19.30, 18.96, 14.13, 11.88; Elemental analysis: calculated for $C_{49}H_{71}NO_4$(%): C, 79.74; H, 9.70; N, 1.90; found: C, 79.57, H; 9.56,N; 1.78.

Compound 1i: Pale yellow crystalline solid, yield: 86.6%, IR (KBr, ν_{max}, cm^{-1}): 3040, 2951,2924, 2868, 2852, 1759, 1624, 1508, 842; ^{1}H-NMR ($CDCl_3$, 400 MHz): δ(ppm) = 8.48 (s, 1H, CH=N), 7.91-7.94 (d, 2H, J = 8.4 Hz, Ar-H), 7.30-7.32 (d, 2H, J = 8.8 Hz, Ar-H), 7.23-7.25 (d, 2H, J = 9.2 Hz, Ar-H), 6.93-6.95 (d, 2H, J = 9.2 Hz, Ar-H), 5.44-5.45 (m, 1H, -C=CH-), 4.58-4.66 (m, 1H, -OCH-CH_2), 3.97-4.01 (t, 2H, -CH_2-O-Ar), 2.50-2.52 (q, 2H, -OCH-CH_2), 0.70-2.05 (m, 60H, -CH, -CH_2 and -CH_3); ^{13}C NMR ($CDCl_3$,400MHz): δ(ppm) = 157.98 (CH=N), 156.82, 153.04, 152.56 (-O-COO-), 144.46, 139.09, 134.24, 129.72, 123.30, 122.19, 121.43, 114.99, 79.12, 68.31, 56.69, 56.13, 49.98, 42.33, 39.71, 39.53, 37.94, 36.84, 36.57, 36.19, 35.80, 31.92, 31.85, 29.60, 29.58, 29.34, 29.32, 28.24, 28.04, 27.65, 26.07, 24.30, 23.84, 22.84, 22.70, 22.58, 21.07, 19.30, 18.96, 14.14, 11.87; Elemental analysis: calculated for $C_{51}H_{75}NO_4$(%): C, 79.95; H, 9.87; N, 1.83; found: C, 79.64, H; 9.70,N; 1.68.

Compound 1j: Pale yellow crystalline solid, yield: 75.8%, IR (KBr, ν_{max}, cm^{-1}): 3038, 2952, 2853, 1757, 1624, 1505, 884; ^{1}H-NMR ($CDCl_3$, 400 MHz): δ(ppm) = 8.48 (s, 1H, CH=N), 7.91-7.94 (d, 2H, J = 8.8 Hz, Ar-H), 7.30-7.32 (d, 2H, J = 8.8 Hz, Ar-H), 7.23-7.25 (d, 2H, J = 8.8 Hz, Ar-H), 6.93-6.95 (d, 2H, J = 8.8 Hz, Ar-H), 5.44-5.45 (m, 1H, -C=CH-), 4.58-4.66 (m, 1H, -OCH-CH_2), 3.97-4.00 (t, 2H, -CH_2-O-Ar), 2.49-2.52 (q, 2H, -OCH-CH_2), 0.70-2.05 (m, 64H, -CH, -CH_2 and -CH_3); ^{13}C NMR ($CDCl_3$,400MHz): δ(ppm) = 157.97 (CH=N), 156.83, 153.04, 152.56 (-O-COO-), 144.46, 139.09, 134.24, 129.72, 123.30, 122.19, 121.43, 114.99, 79.12, 68.32, 56.71, 56.13, 49.98, 42.33, 39.71, 39.53, 37.94, 36.84, 36.57, 36.19, 35.80, 31.92, 31.85, 29.69, 29.60, 29.57, 29.38, 29.32, 28.24, 28.04, 27.64, 26.10, 24.30, 23.84, 22.84, 22.70, 22.58, 21.07, 19.30, 18.96, 14.1, 11.87; Elemental analysis: calculated for $C_{53}H_{79}NO_4$(%): C, 80.15; H, 10.03; N, 1.76; found: C, 79.96, H; 9.77,N; 1.53.

Compound 1k: Pale yellow crystalline solid, yield: 78.2%, IR (KBr, ν_{max}, cm^{-1}): 3020, 2922, 2852, 1757, 1624, 1505, 834; ^{1}H-NMR ($CDCl_3$, 400 MHz): δ(ppm) = 8.48 (s, 1H, CH=N), 7.91-7.94 (d, 2H, J = 8.8 Hz, Ar-H), 7.30-7.32 (d, 2H, J = 8.4 Hz, Ar-H), 7.23-7.25 (d, 2H, J = 8.8 Hz, Ar-H), 6.93-6.95 (d, 2H, J = 8.8 Hz, Ar-H), 5.44-5.45 (m, 1H, -C=CH-),

4.58-4.66 (m, 1H, -OCH-CH_2), 3.97-4.01 (t, 2H, -CH_2-O-Ar), 2.49-2.52 (q, 2H, -OCH-CH_2), 0.70-2.05 (m, 68H, -CH, -CH_2 and -CH_3); ^{13}C NMR ($CDCl_3$,400MHz): δ(ppm) = 157.99 (CH=N), 156.81, 153.04, 152.57 (-O-COO-), 144.46, 139.09, 134.24, 129.72, 123.30, 122.19, 121.42, 114.99, 79.12, 68.31, 56.69, 56.13, 49.98, 42.33, 39.72, 39.53, 37.94, 36.84, 36.57, 36.19, 35.81, 31.94, 31.85, 29.71, 29.70, 29.68, 29.63, 29.61, 29.44, 29.39, 29.32, 28.24, 28.04, 27.65, 26.07, 24.30, 23.84, 22.85, 22.71, 22.57, 21.08, 19.30, 18.96, 14.14, 11.87; Elemental analysis: calculated for $C_{55}H_{83}NO_4$(%): C, 80.34; H, 10.17; N, 1.70; found: C, 79.22, H; 9.98,N; 1.56.

Compound 1l: Pale yellow crystalline solid, yield: 88.4%, IR (KBr, ν $_{max}$, cm^{-1}): 3030, 2953, 2855, 1761, 1625, 1506, 834; ^{1}H-NMR ($CDCl_3$, 400 MHz): δ(ppm) = 8.48 (s, 1H, CH=N), 7.91-7.94 (d, 2H, J = 8.8 Hz, Ar-H), 7.30-7.32 (d, 2H, J = 8.8 Hz, Ar-H), 7.23-7.25 (d, 2H, J = 8.8 Hz, Ar-H), 6.93-6.95 (d, 2H, J = 8.8 Hz, Ar-H), 5.44-5.45 (m, 1H, -C=CH-), 4.61-4.64 (m, 1H, -OCH-CH_2), 3.97-4.00 (t, 2H, -CH_2-O-Ar), 2.50-2.51 (q, 2H, -OCH-CH_2), 0.70-2.05 (m, 72H, -CH, -CH_2 and -CH_3); ^{13}C NMR ($CDCl_3$,400MHz): δ(ppm) = 157.98 (CH=N), 156.79, 153.04, 152.57 (-O-COO-), 144.46, 139.09, 134.24, 129.72, 123.30, 122.19, 121.42, 114.99, 79.12, 68.34, 56.69, 56.13, 49.98, 42.33, 39.72, 39.50, 37.92, 36.83, 36.57, 36.19, 35.81, 31.94, 31.85, 29.71, 29.70, 29.68, 29.63, 29.61, 29.56, 29.42, 29.36, 29.31, 28.24, 28.04, 27.65, 26.07, 24.30, 23.84, 22.85, 22.71, 22.57, 21.08, 19.30, 18.96, 14.13, 11.87; Elemental analysis: calculated for $C_{57}H_{87}NO_4$(%): C, 80.51; H, 10.31; N, 1.65; found: C, 80.34, H; 10.19, N; 1.48.

Compound 1m: Pale yellow crystalline solid, yield: 89.9%, IR (KBr, ν $_{max}$, cm^{-1}): 3028, 2953, 2920, 2850, 1757, 1624, 1508, 831; ^{1}H-NMR ($CDCl_3$, 400 MHz): δ(ppm) = 8.48 (s, 1H, CH=N), 7.91-7.94 (d, 2H, J = 8.8 Hz, Ar-H), 7.30-7.32 (d, 2H, J = 8.8 Hz, Ar-H), 7.23-7.25 (d, 2H, J = 8.8 Hz, Ar-H), 6.93-6.95 (d, 2H, J = 8.8 Hz, Ar-H), 5.44-5.45 (m, 1H, -C=CH-), 4.61-4.64 (m, 1H, -OCH-CH_2), 3.97-4.00 (t, 2H, -CH_2-O-Ar), 2.50-2.53 (q, 2H, -OCH-CH_2), 0.70-2.05 (m, 76H, -CH, -CH_2 and -CH_3); ^{13}C NMR ($CDCl_3$,400MHz): δ(ppm) = 157.98 (CH=N), 156.81, 153.04, 152.57 (-O-COO-), 144.46, 139.09, 134.24, 129.72, 123.30, 122.19, 121.42, 114.99, 79.12, 68.34, 56.69, 56.13, 49.98, 42.33, 39.72, 39.50, 37.92, 36.83, 36.57, 36.19, 35.81, 31.96, 31.87, 31.42 29.71, 29.70, 29.68, 29.63, 29.61, 29.56, 29.44, 29.37, 29.31, 28.24, 28.04, 27.65, 26.07, 24.30, 23.84, 22.85, 22.71, 22.57, 21.08, 19.30, 18.96, 14.13, 11.87. Elemental analysis: calculated for $C_{59}H_{91}NO_4$(%): C, 80.68; H, 10.44; N, 1.59; found: C, 80.46, H; 10.23, N; 1.35.

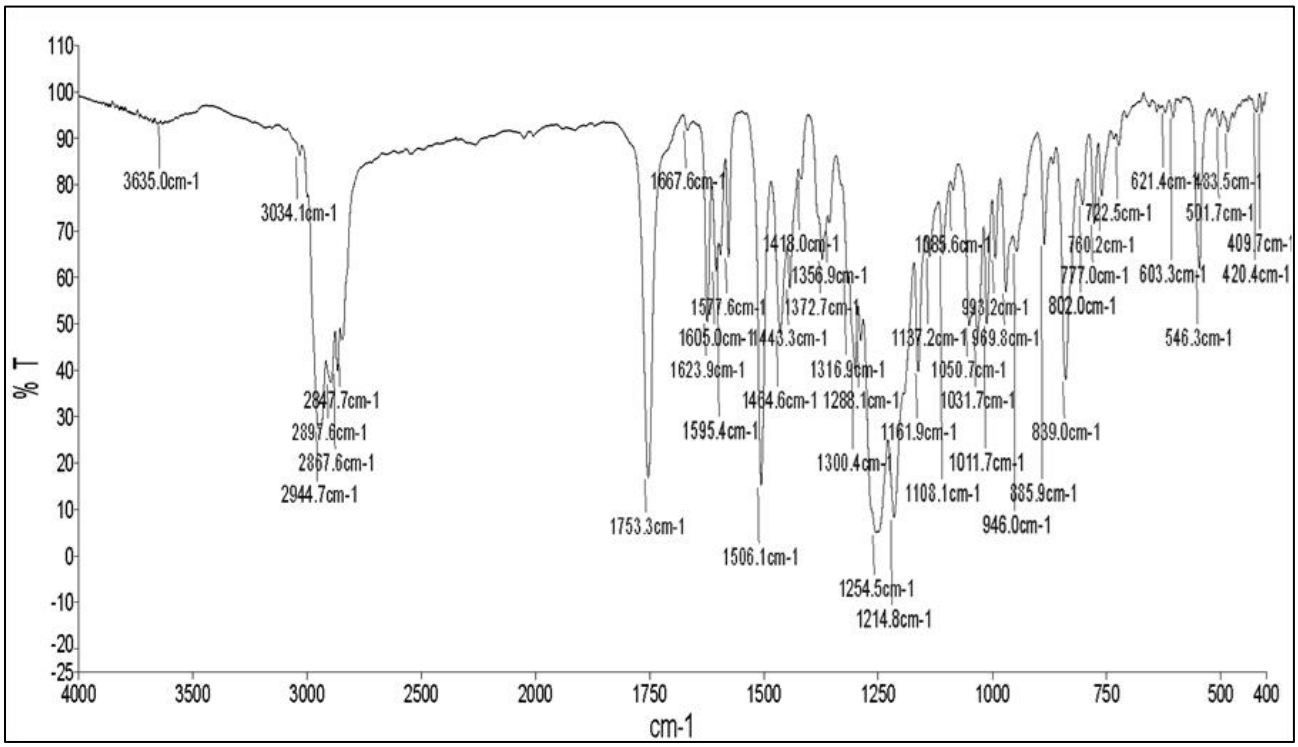

Figure 2.3 (a): FT-IR spectra of **Compound 1a**

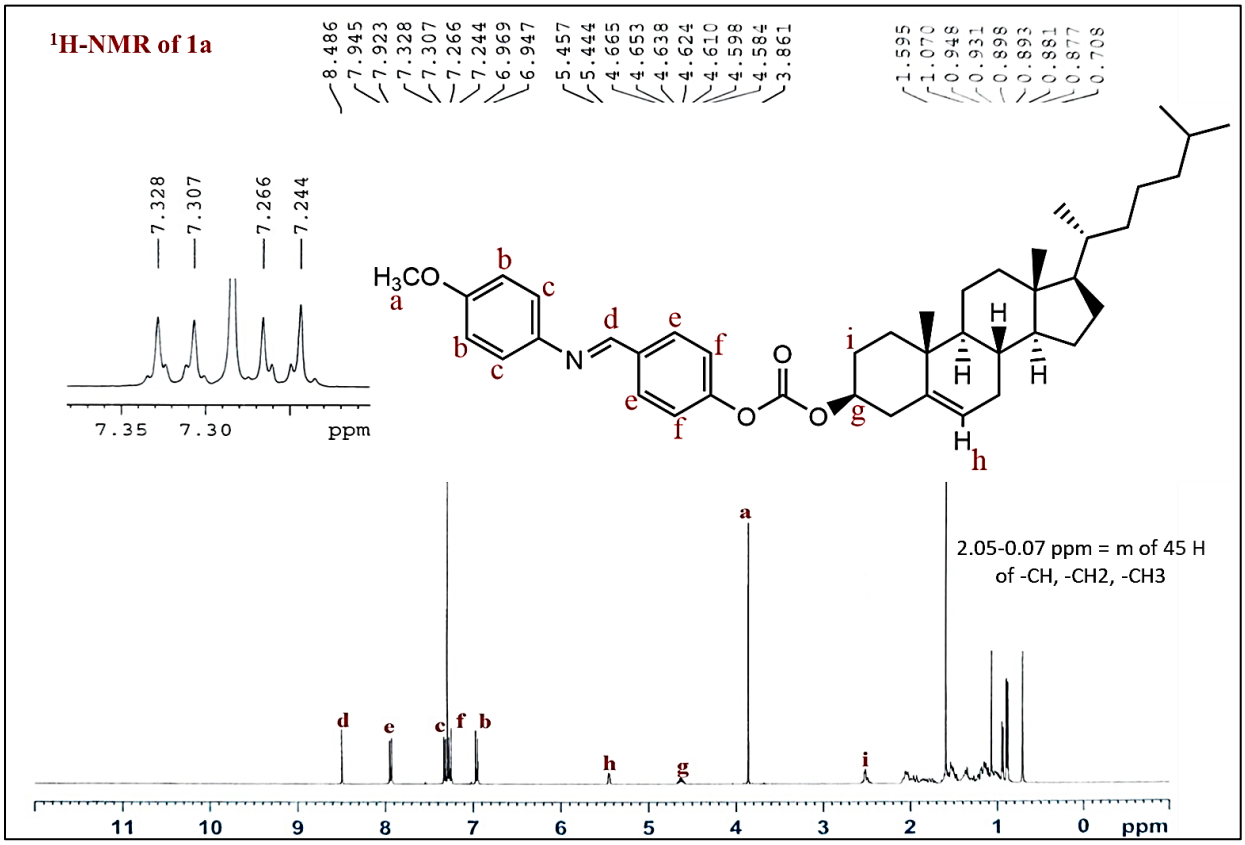

Figure 2.3 (b): ^{1}H-NMR spectra of **Compound 1a**

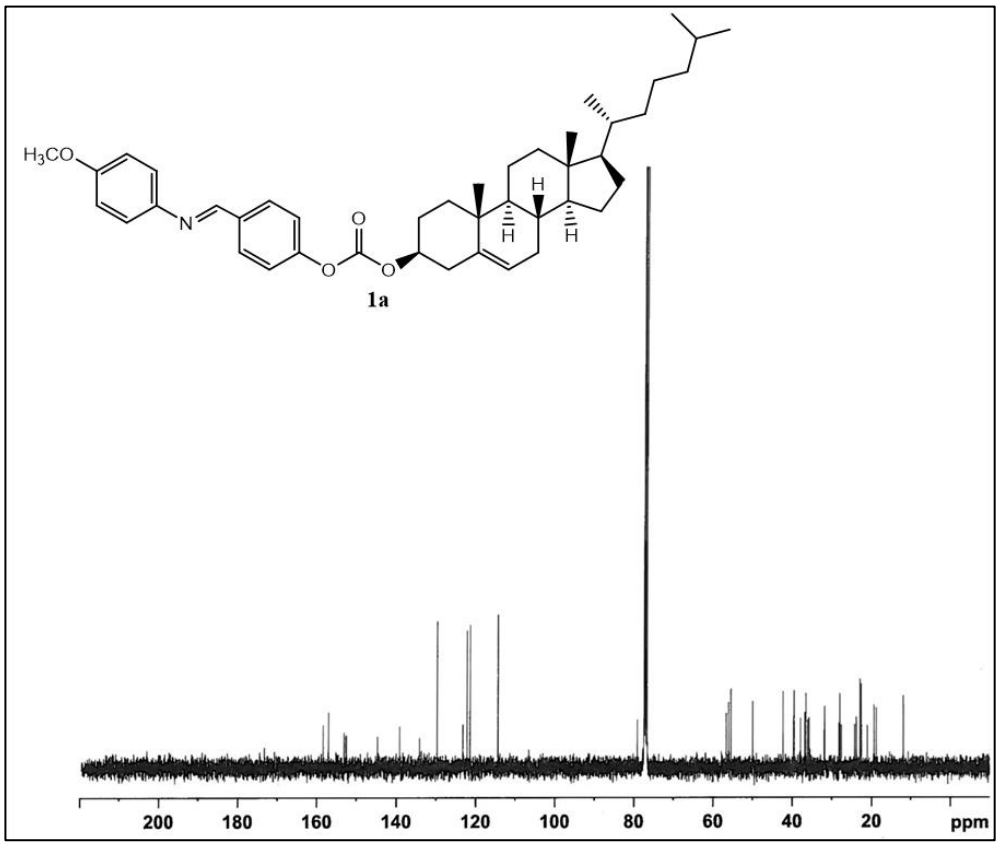

Figure 2.3 (c): ^{13}C-NMR spectra of **Compound 1a**

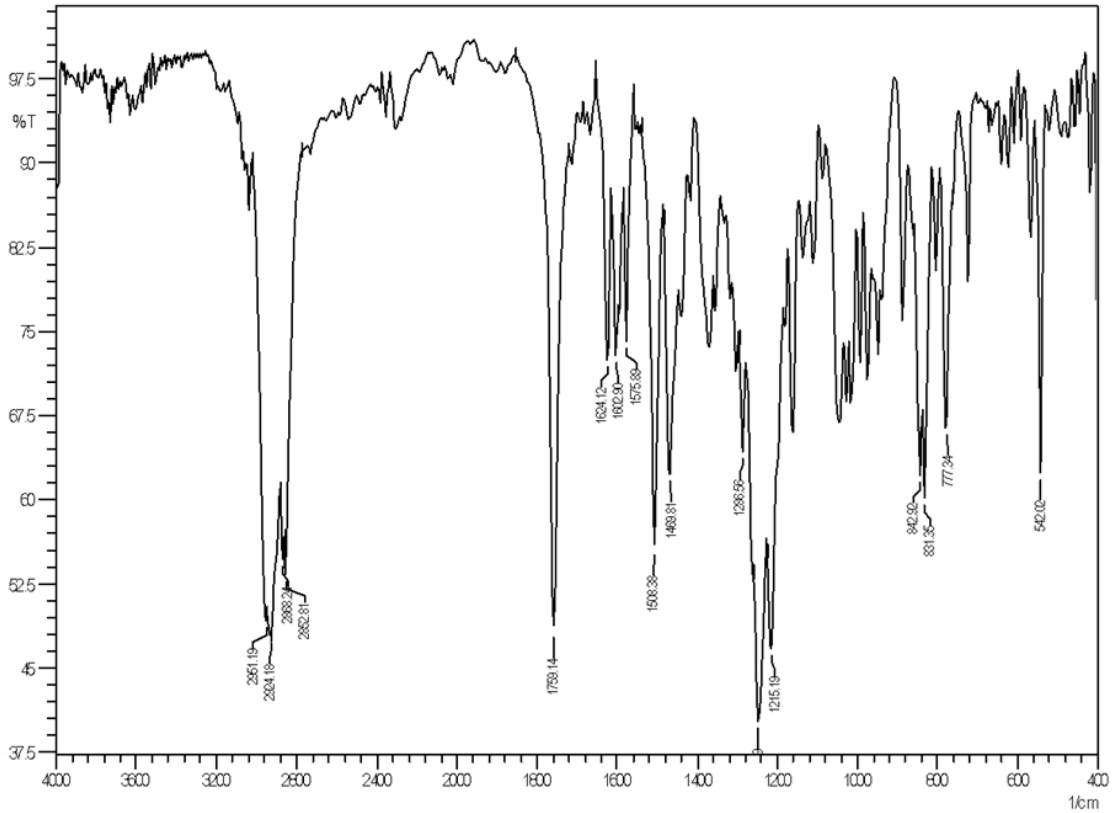

Figure 2.4 (a): FT-IR spectra of **Compound 1i**

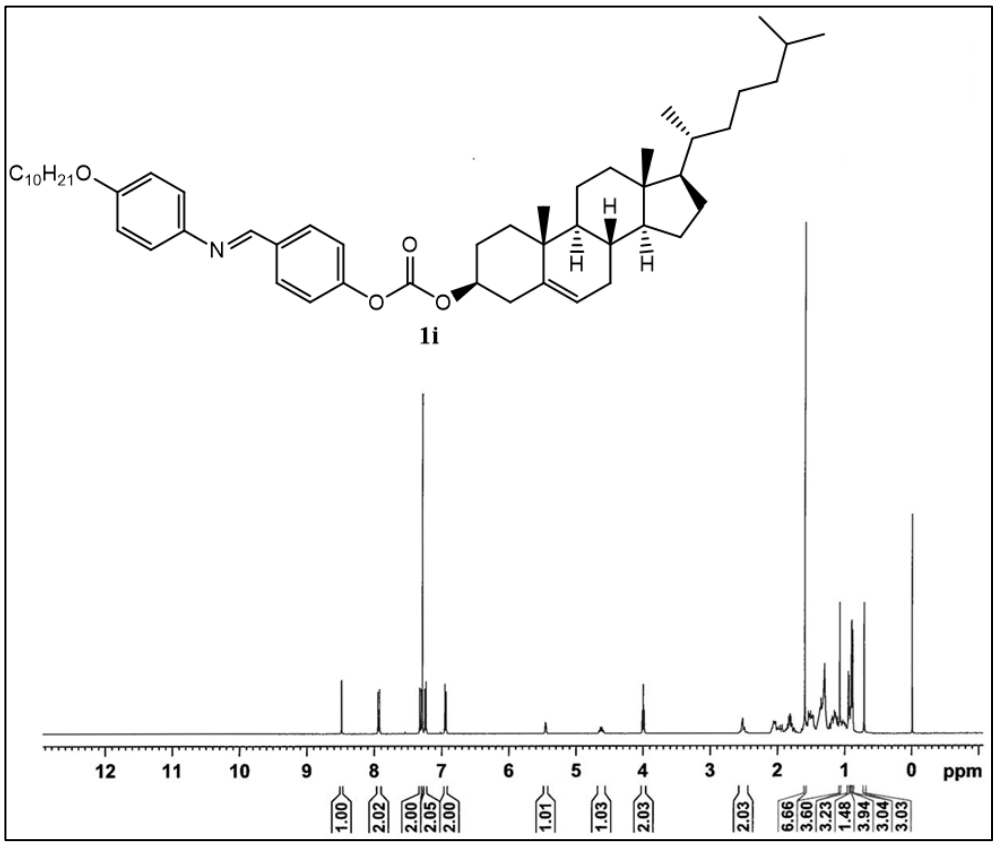

Figure 2.4 (b): ^{1}H-NMR spectra of **Compound 1i**

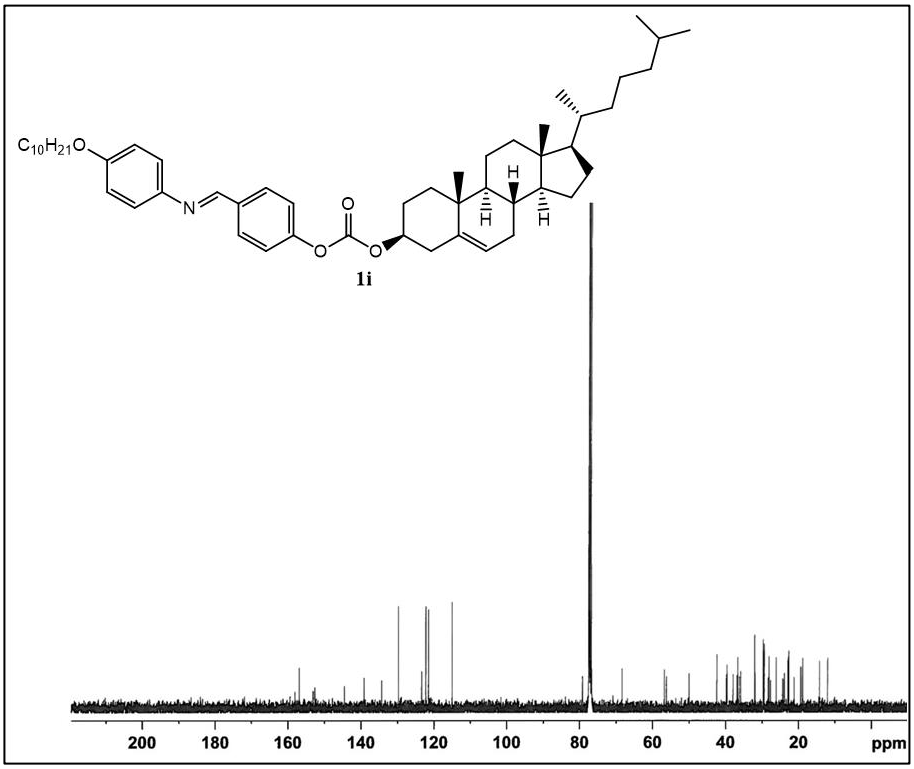

Figure 2.4 (c): ^{13}C-NMR spectra of **Compound 1i**

2.3. Results and discussion

The final Schiff's base derivatives **(1a-m)** were prepared by reaction of 4-formyl phenyl cholesteryl carbonate **(4)** with the appropriate 4-n-alkoxy aniline **(7a-m)**. The synthetic route adopted is given in Scheme 2.1. All the compounds in the series exhibit mesomorphic properties. The methyl to n-butyl derivatives of Series I show oily streaks texture of cholesteric (cholesteric) phase. The n-pentyl and n-hexyl derivatives show oily streaks of the N* phase, while on cooling, in addition to cholesteric phase, they also show the SmA mesophase. The n-heptyl to n-decyl compounds show enantiotropic SmA-N*-Iso transition. The SmA to N* transition is accompanied by an interceding TGB_A phase. The n-dodecyl derivative shows only enantiotropic SmA phase. The higher derivatives from n-tetra decyl to n-octa decyl show enantiotropic SmC*-SmA-Iso transition. The DSC thermograms are in comparable agreement with the polarising optical microscopy. Compounds were also thermally stable up to 330-350°C as analyzed thermogravimetrically.

The FT-IR and NMR spectra, as well as the elemental analyses, are in complete agreement with the structure. In IR spectra, the compound 4-formyl phenyl cholesteryl carbonate **(4)** displays prominent bands (ν_{max}, cm^{-1}) at 2943, 2888, 2868,2851 (CH aliphatic), 2720 (CH stretch aldehyde), 1755 (CO carbonate), 1703 (CO stretch aldehyde), 1450-1500 (Ph), 1575 cm^{-1} (C-C aromatic) stretch. The compound **(1a)** exhibits major IR bands at 2944, 2897, 2867, 2847 (CH aliphatic), 1753 (CO carbonate), and 1623 (C=N azomethine) after condensation with 4-methoxy anilines. The disappearance of bands at 1703 and 2720 cm^{-1} due to aldehyde (CHO) and the appearance of a new band at 1623 cm^{-1} due to azomethine (CH=N) indicate condensation of aldehyde with amine to form Schiff base, thereby confirming the structure of the compound 4,4'-methoxy benzylidene phenyl cholesteryl carbonate **(1a)**.

The proton NMR of compound **4** displayed a prominent signal at δ 9.91 (s, 1H, CHO) ppm of the aldehyde group. The proton NMR of the final Schiff's base 4,4'-methoxy benzylidene phenyl cholesteryl carbonate **(1a)** depicts signals at δ 8.48 (s, 1H, CH=N), δ 7.94-6.94 (m, 8H, Ar-H), δ 5.5 (d, 1H, olefinic H in cholesterol), δ 4.6 (m, 1H, H of cholesterol near carbonate linkage), δ 3.86 (s, 3H, $-OCH_3$), δ 2.5 (d, 2H, $-OCH-CH_2$), δ 2.05-0.70 (m, 41H, -CH,$-CH_2$ and $-CH_3$ of cholesterol) ppm, respectively. The disappearance of the singlet at δ 9.91 ppm and appearance of a characteristic signal due to the azomethine group at δ 8.48 ppm confirm the formation of 4,4'-methoxy benzylidene phenyl cholesteryl carbonate **(1a)**. The ^{13}C NMR spectrum of the compound **(4)** depicts prominent peaks at δ 191.2 (CHO) and δ 150.1(-O-COO-) ppm, whilst the compound **(1a)** exhibits signal at δ 158.36 (azomethine carbon

CH=N), δ 152.56 (carbonate carbon -O-COO-), and δ 129.75-114.40 (carbons of aromatic rings) ppm. Thus, the appearance of azomethine carbon (CH=N) **(1a)** at δ 158.36 ppm confirms the formation of Schiff base **(1a)**.

All other members of the series **(1b-1m)** exhibit similar IR, NMR (^{1}H and ^{13}C) bands and are listed in the synthesis.

2.3.1. Texture analysis

To investigate the liquid crystalline behavior of the synthesized compounds, the compounds were sandwiched between two untreated glass slides, and optical texture investigations were performed on heating and cooling cycles using an optical polarizing microscope equipped with a heating stage. During the repeated heating and cooling processes, all the compounds remained stable. All the synthesized compounds are mesogenic in nature. In the series of compounds, the lower homologous from **1a-1d** melted and exhibited a typical oily streaks texture of cholesteric [48] (chiral nematic mesophase) phase **Figure 2.5 (a)** that maintained until the compounds became isotropic. As it cooled from isotropic melt, the droplet cholesteric texture exhibited and gradually coalesced into the cholesteric schlieren texture. It belonged to thermotropic enantiotropic chiral nematic LCs. Compounds **1e** and **1f** on heating showed oily streaks of the cholesteric phase until isotropic, similar to **1a-1d** while on cooling from isotropic melt, in addition to the cholesteric phase, a dark-field view of the SmA mesophase was also observed, which proceeds through a TGB_A phase. The compounds **1g-1i** displayed an enantiotropic N* and smectic phase seen as black area because here the optic axis is oriented along the direction of light propagation [49], with an interceding TGB_A phase. The Cr-Sm transition is easily visible in the DSC thermogram, while the transition involving the Sm-TGB_A mesophase **Figure 2.5 (b)** which is associated with the minimal enthalpy change, is not witnessed in the DSC thermogram, but this transitory TGB_A phase is evidenced optically by their typical filament texture as observed under the cross polarizers [50,51]. The dodecyl derivative **1j** exhibited only an enantio-tropic Smectic A mesophase **Figure 2.5 (c)**. The higher derivatives **1k-1m** on the heating cycle first exhibited the SmC* mesophase, which on further heating changes from tilted helical structure to the untwisted parallel structure of the SmA phase observed as fan shaped texture and maintained until isotropic. On cooling from isotropic melt, the compounds exhibited SmA phase **Figure 2.5 (d)**, even though not observed from DSC, on further cooling from SmA phase under POM, these compounds exhibited broken fan shaped texture with equidistant line pattern due to the helical superstructure resembling SmC*

mesophase **Figure 2.5 (e)** throughout a somewhat large temperature range which resembles the textures observed in the literature [52–54].

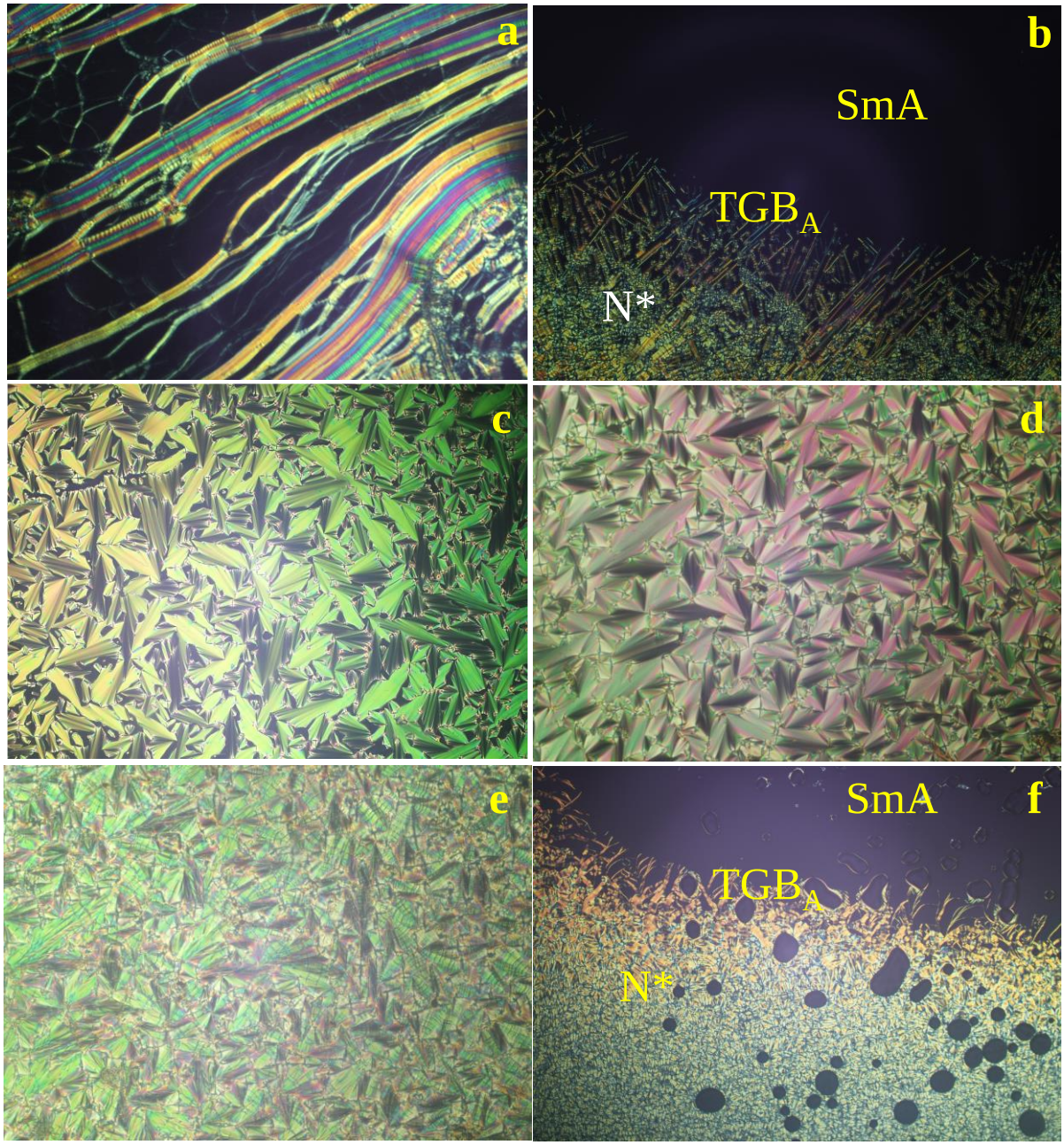

Figure 2.5: Microphotographs of the textures observed under POM for the different LC phases of compounds placed between two untreated glass substrates **(a)** Oily streaks texture of cholesteric or chiral nematic (N*) phase of **1b** at 179°C, **(b)** SmA-TGB$_A$-N* transition of **1h** at 256°C, **(c)** focal conic texture of SmA mesophase of **1j** at 250°C, **(d)** fan shaped texture of SmA mesophase of **1l** at 249°C, **(e)** broken fan shaped texture with helix lines of SmC* phase of **1l** at 113°C, **(f)** filament texture of SmA-TGB$_A$-N* transition of **10i** at 260°C

Table 2.1: Phase transition temperature of compounds **1a-m** [a, b]

Sample code	No. of C	Heating Temp °C [ΔH kJ mol^{-1}]	Cooling Temp °C [ΔH kJ mol^{-1}]
1a	1	Cr 146.6[33.69] N* 294.9[0.41] I	I 288.0[0.29] N* 82.9[26.70] Cr
1b	2	Cr 174.8[42.98] N* 305.8[0.87] I	I 298.6[0.74] N* 79.6[36.54] Cr
1c	3	Cr 223.3[34.48] N* 285.1[0.78] I	I 277.2[0.66] N* 99.4[26.34] Cr
1d	4	Cr 249.9[46.29] N* 289.6[1.14] I	I 285.0[0.83] N* 130.0[40.36] Cr
1e	5	Cr 257.2[52.14] N* 284.6[0.96] I	I 276.2[0.82] N* (197.5) [0.90] TGB$_A$-SmA [c,d] 100.2[58.04] Cr
1f	6	Cr 260.5[31.99] N* 282.0[0.87] I	I 274.8[0.94] N* (218.4) [0.76] TGB$_A$-SmA [c,d] 104.0[36.15] Cr
1g	7	Cr 224.5[32.27] SmA- TGB$_A$[c,d] 259.8[1.19] N* 281.4[1.01] I	I 277.7[0.95] N* 256.9[1.04] TGB$_A$-SmA[c,d] 67.5[26.13] Cr
1h	8	Cr 254.4[48.11] SmA- TGB$_A$[c,d] 258.8[0.72] N* 274.6[1.08] I	I 268.7[1.53] N* 248.9[0.77] TGB$_A$-SmA[c,d] 76.8[52.16] Cr
1i	10	Cr 253.8[23.85] SmA- TGB$_A$[c,d] 260.3[0.37] N* 270.1[1.06] I	I 267.8[1.23] N* 257.4[0.41] TGB$_A$-SmA[c,d] 74.9[33.09] Cr
1j	12	Cr 260.2[18.68] SmA 267.7[10.93] I	I 259.7[12.06] SmA 71.6[36.61] Cr
1k	14	Cr 137.2[28.19] SmC*[d] 250.6 SmA 265.6[31.76] I	I 264.6[29.22] SmA 110.0 SmC*[d] 96.4[37.53] Cr
1l	16	Cr 133.8[26.37] SmC*[d] 248.8 SmA 257.9[20.44] I	I 252.2[22.65] SmA 117.9 SmC* 100.3[28.08] Cr
1m	18	Cr 128.9[16.86] SmC*[d] 230.6 SmA 251.4[11.04] I	I 245.1[16.86] SmA 121.1 SmC*[d] 91.6[21.72] Cr

Temperature in parenthesis ( ) indicates monotropic transition; Cr = crystal, SmA = smectic A phase, SmC* = chiral smectic C phase, N* = chiral nematic/ cholesteric phase, TGB$_A$ = twist grain boundary A phase, I = isotropic temperature.

[a]Phase transition temperatures were determined/confirmed by both Polarising optical microscope (POM) and differential scanning calorimetry (DSC) studies: peak temperatures in the DSC thermograms obtained during the first heating and cooling cycles (scanning rate = 5°C min^{-1}) coupled with POM measured temperatures are given; [b]Transition temperatures of some of the compounds were determined with the aid of a POM study as the expected well-resolved thermograms of both heating and cooling cycles could not be obtained; [c]Although TGB$_A$–SmA/

SmA–TGB_A phase transitions were observed in POM, they were not resolved in DSC traces; hence the enthalpy value represents the combined enthalpy for TGB_A–SmA/ SmA–TGB_A transitions; [d]Phase transition was observed under POM; enthalpy change too weak to be detected by DSC.

2.3.2. Thermal properties

The phase transition temperatures, enthalpy variations, and mesophase textures of the pure compounds **1a-m** are summarized in **Table 2.1**. DSC curves as in **Figure 2.6 (a** and **b)** and POM observations provided clear transition temperatures and textures for all of the compounds, and they were in reasonable agreement with each other over the many heating/cooling cycles. Compounds **1a-d** displayed two endotherms from crystalline solid to chiral nematic phase (Cr-N*) and chiral nematic phase to isotropic liquid phase (N*-Iso) on heating. Similarly, on cooling, two exotherms were observed, corresponding to isotropic liquid phase to chiral nematic phase (Iso-N*) and chiral nematic phase to crystalline solid state (N*-Cr). Compounds **1e** and **1f** showed two endotherms from the heating cycle and three exotherms on cooling cycle, while on heating, the first transition was observed from crystalline solid to chiral nematic mesophase (Cr-N*), and the second transition was observed for chiral nematic mesophase to isotropic liquid phase (N*-Iso). In the cooling cycle, three exotherms correspond to isotropic liquid phase to chiral nematic phase (Iso-N*), nematic to smectic A phase (N*-SmA) interceding with TGB_A, and smectic A phase to crystalline solid (SmA-Cr). Compounds **1g-i** showed three exotherm and three endotherm peaks corresponding to crystal to twist grain boundaries A-smectic A (Cr- TGB_A-SmA), twist grain boundaries A-smectic A- chiral nematic (TGB_A-SmA-N*) and chiral nematic-isotropic (N*-Iso) in both heating and cooling cycles. Compound **1j** exhibited enantiotropic mesophase with two endotherm and two exotherm peaks for the crystal-smectic A (Cr-SmA) and smectic A-isotropic (SmA-Iso) transitions. Compound **1k-m** showed two endotherm and two exotherm peaks for crystal-smectic A (Cr-SmA) and smectic A-isotropic transition (SmA-Iso). An additional SmC* phase was observed for **1k-m** using polarising optical microscopy but was not detected in DSC as it is associated with the minimal enthalpy change.

Enthalpy changes are fairly predicted during the initial transition of crystal-chiral nematic/smectic A phase for all of the compounds indicated in **Table 2.1**. The enthalpy changes during the chiral nematic-isotropic transition, on the other hand, are smaller than predicted. Again, this is to be expected with these sorts of mesogens [55].

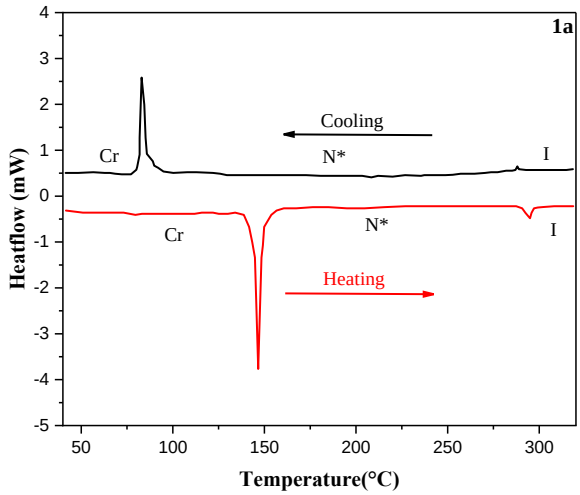

Figure 2.6 (a): DSC thermogram of **1a**

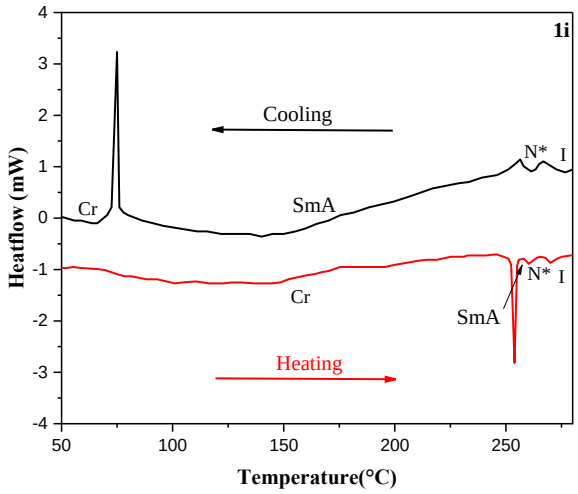

Figure 2.6 (b): DSC thermogram of **1i**

The Smectic A (SmA) and TGB_A (twist grain boundary A) phases typically do not show an enthalpy change because the transitions between these phases are due to competing intermolecular interactions and strong molecular chirality, as observed in the thermograms of compounds **1e-i.** Likewise, for the transition from Smectic A (SmA) where the molecules are uniformly aligned to each other in the layers to Smectic C* (SmC*) where they exhibit a tilted orientation, the primary change occurs in the molecular arrangement and orientation within the layers rather than a disruption or forming of the interactions, which does not involve a substantial enthalpy change as observed in thermograms for compound **1k-m**.

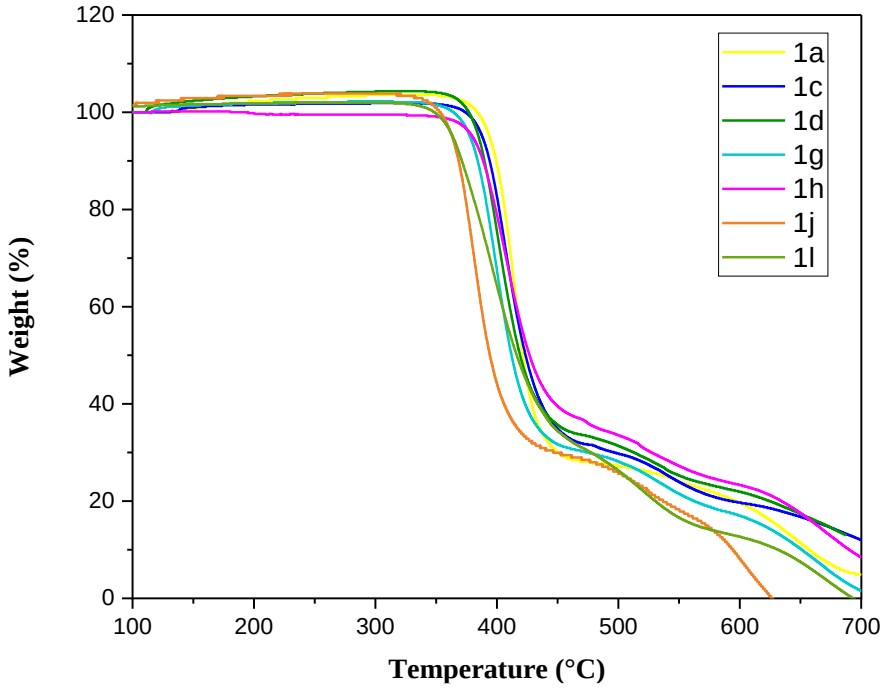

Figure 2.7: TGA profile for some of the cholesterol derivatives

Compounds **1a,1c,1d,1g,1h,1j** and **1l** were subjected to thermogravimetric analysis (TGA) in order to comprehend the thermal stability. While examining the mesomorphic behaviour, it was discovered that all the cholesterol derivatives were stable up to 330-350°C, ruling out the possibility of thermal decomposition of these derivatives **(Figure 2.7)**. However, due to extremely high isotropic temperatures, repeated heating and cooling of the cholesterol derivatives caused decomposition.

2.3.3. Structure-mesomorphic property relationship

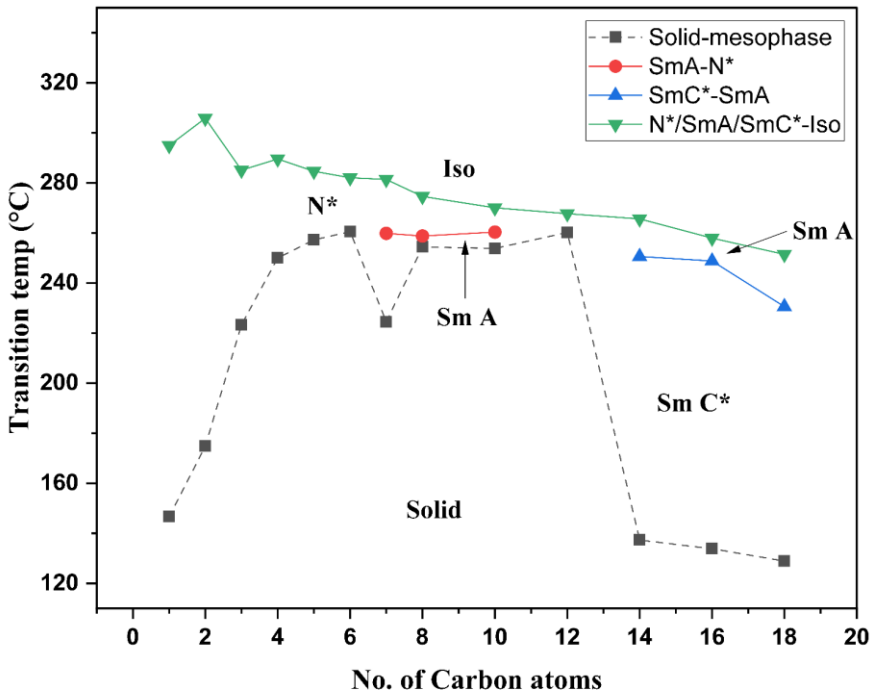

Figure 2.8: Plot of transition temperatures (°C) versus number of carbon atoms in the alkoxy chain for compounds **1 a-m**

A graphic illustration of transition temperature versus number (n) of C atoms in the alkyl chains is shown in **Figure 2.8**. Based on **Figure 2.8**, the transition curves Cr-mesophase, SmA-N*, SmC*-SmA and N*/SmA/SmC*-Iso were obtained. The N*/SmA/SmC* to isotropic transition temperatures exhibits a sharp falling tendency and shows distinct odd-even effect only for the first five members of the series, while the SmA to N* transition shows an ascending trend with increasing terminal chain length. The SmC* to SmA transition shows a rising tendency with increasing terminal chain length. The curve of the Cr to first mesophase rises to maximum till the dodecyl derivative and then a falling tendency is observed till the octadecyl derivative except for the heptyl derivative which may be due to the commencement of the SmA phase. The nematic-isotropic transition temperature tends to decrease as terminal group span

increases in Series I, and the onset of smectic mesophase from medieval homologue is also a common trend. In a system like this, this specific pattern is expected [56,57]. Lower homologues exhibit minimal separation within the aromatic nuclei and maximal terminal cohesion, leading to them being entirely nematogens. As we advance through the series, lateral cohesive forces increase, causing molecules to align themselves in a encrusted structure formerly transitioning into the nematic mesophase. As terminal intermolecular interactions are relatively weak to preserve the parallel molecular orientation, smectogenic properties should predominate at the expense of nematic phase stability as terminal chain length increases.

Organic compounds have a close association amid their molecular structure as well as their liquid crystalline characteristics, which in turn influences their thermal stability. One can establish a correlation between these compounds' liquid crystalline characteristics and a measurement of thermal stability by looking at their molecular constitution. Thermal stabilities across various mesogenic series are compared in terms of their average values **Table 2.2**.

Comparison of molecular structure of present **Series I** with reported series:

(1) 4,4´-alkoxy benzylidene amino cholesteryl carbonate; **Series I**

(2) "Cholesteryl 4-n-alkoxybenzylidene-4´-aminobenzoates"; **Series A** [58]

(3) "Cholesteryl 4-(4´-n-alkoxy benzoyl) amido benzoates"; **Series B** [59]

Figure 2.9 illustrates the geometry of these compounds.

Table 2.2: Average thermal stabilities (°C) of Series I, A and B compounds.

Series	**I**	**A**	**B**
N*- Iso	291.0	321.0	327
	($C_{1\text{-}6}$)	($C_{1\text{-}6}$)	($C_{1\text{-}6}$)
SmA/SmC*- N*	259.6	196	235.3
	($C_{7,8,10}$)	($C_{7\text{-}10}$)	($C_{7,8,10}$)

The compounds in Series I contains the formyl cholesteryl carbonate moiety linked to n-alkoxy aniline, which forms an azomethine linkage, while in Series A the p-aminobenzoate of cholesterol is linked to n-alkoxy benzaldehydes to form the Schiff's base linkage. The higher N* - Iso thermal stability of Series A can be attributed to the central ester linkage compared to carbonate in Series I. Compared to esters, carbonates often exhibit lower mesophase temperatures and a wider range of mesophases due to the carbonate group's relatively flexible character compared to the esters more rigid structure. While the higher thermal stability of the SmA/SmC* - N* of Series I may be due to the interceding TGB_A mesophase.

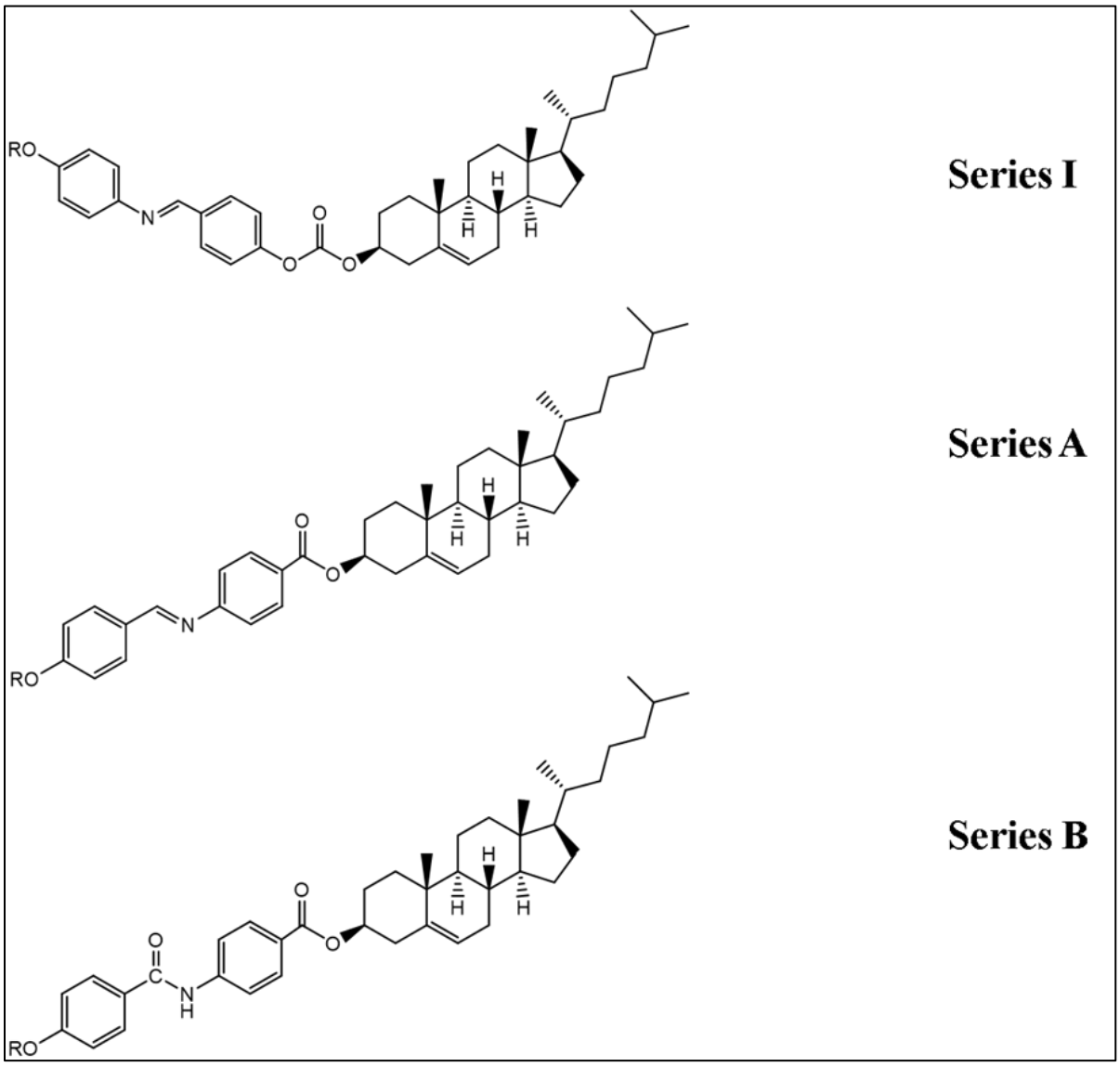

Figure 2.9: The geometric comparison of **Series I, A,** and **B**

The compound in Series I differs from Series B not only in the carbonate and ester linkage but also the reversible central azomethine linkage is replaced by an amide linkage. In comparison to carbonates, the molecule is more rigid due to the presence of the amide linkage. Due to resonance, the amide bond exhibits partial double bond characteristics, which restrict free rotation around the double bond. The mesomorphic characteristics of amides are impacted by this enhanced rigidity. A majority of the time, amides exhibit higher mesophase temperatures than carbonate, which is the case. As the length and symmetry of the substituents increase, the likelihood of the development of ordered mesophases increases, which is also evident as the SmA/SmC*-N* thermal stability of Series B is very close to that of Series I.

As evident, the Chol-Iso average thermic stability of Series B is the highest among all three series, further confirming that amide linkage is more conducive to mesomorphism as

compared to azomethine linkage, while the thermal stability of Series I is the lowest, which may be due to the more flexible carbonate linkage. The forgoing discussion indicates that a slight modification in the linking groups in the molecular structure can adversely affect the mesomorphic properties of the system.

2.3.4. Optical Properties

The ultraviolet-visible absorption spectra of the compounds **1a-m** in $CHCl_3$ solution are shown in **Figure 2.10** and their corresponding photophysical data are mentioned in **Table 2.3**. Due to their structural similarity, the absorption spectra of compounds **1a-m** were all quite similar in shape. In absorbance spectra, the λ_{max} of all the compounds occurred near 339 nm. The highest absorption peaks of all the compounds were found to be near 269 nm. The band at higher energy (269 nm) is due to π- π* transition of benzene ring [60], while the band at lower energy (339 nm) is due to n- π* transition of the azomethine linkage (CH=N), with considerable charge transfer characteristic [61,62]. With the increase in the alkoxy chain length, a slight red shift is observed in most of the compounds. The absorbance is maximum in the case of compound **1e** and for compound **1k** the absorbance is a minimum.

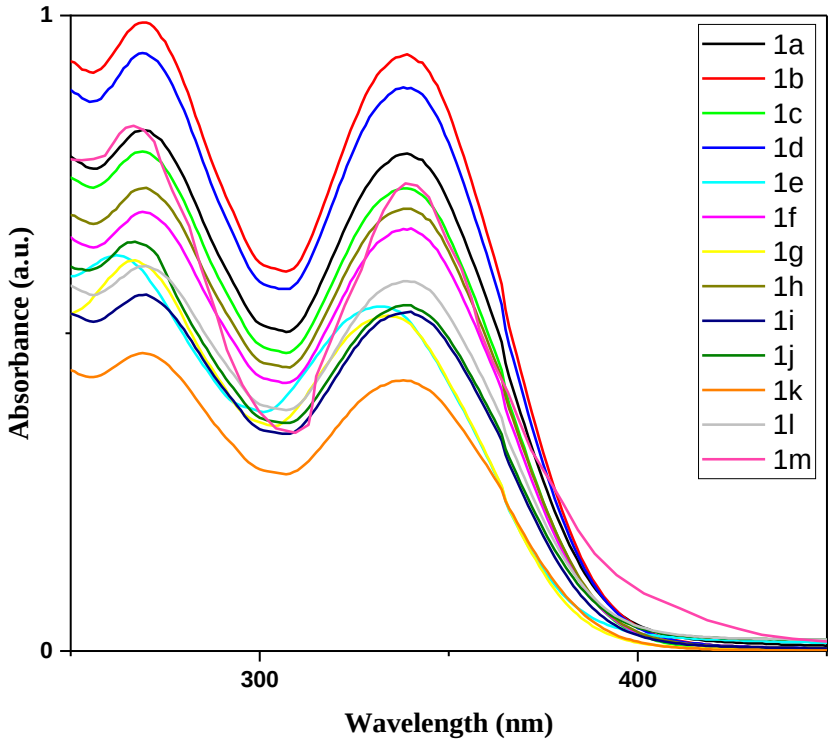

Figure 2.10: UV absorbance spectra of compounds **1a-m**

Photoluminescence (PL) is an important property of liquid crystalline materials used in displays [63]. The photoluminescence spectra of synthesised compounds were done in $CHCl_3$ ($1x10^{-5}$ M) at wavelengths 350-750 nm with an excitation wavelength of 340 nm to investigate the link between structure and spectral characteristics. In all analyses, the emission and excitation bandwidths were set to 5 nm. All the compounds **1a-m** are blue emitters in solution and exhibit essentially the same luminescence profile with three emission peaks as shown in **Figure 2.11,** and their corresponding photophysical data are mentioned in **Table 2.3**.

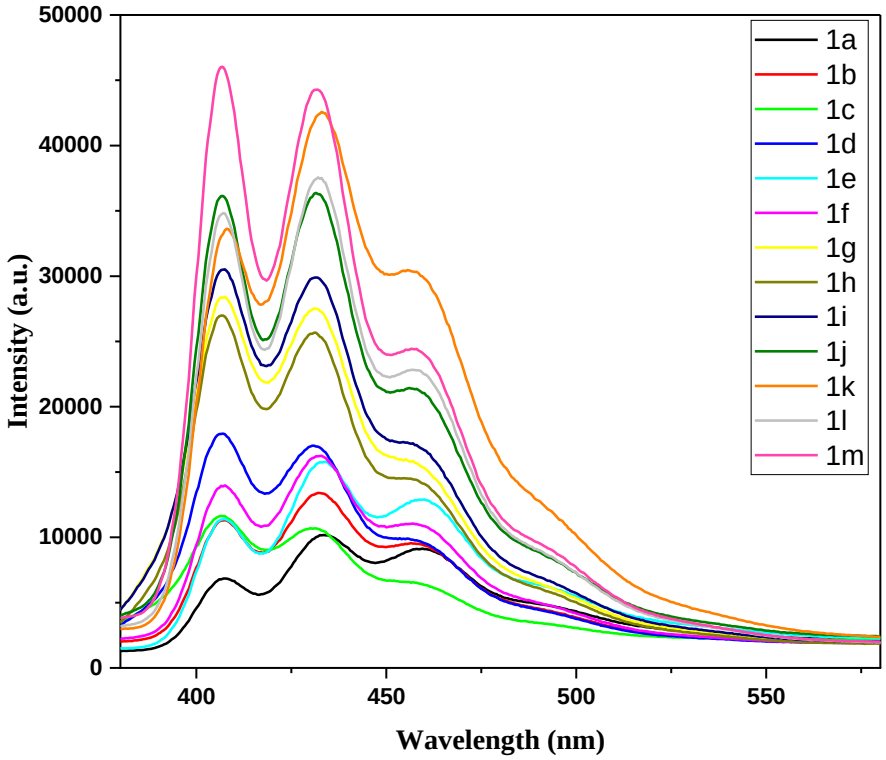

Figure 2.11: Fluorescence spectra of compounds **1a-m** in chloroform ($1x10^{-5}$ M). All of the compounds were excited at 340 nm.

They emit strong fluorescence at wavelength of 400–470 nm. The presence of 4-n-alkoxy group at the terminal end, along with a carbonate linkage, induces an intramolecular charge transfer (ICT) phenomenon in the same direction. The addition of the carbonate group and Schiff's base within the cholesterol moiety impacts this ICT effect, leading to the generation of a fluorescence emission spectrum [64]. With the gradual increase in chain length of the alkoxy group, fluorescence intensity increases continuously. The fluorescence quantum yields in $CHCl_3$ (1×10^{-6} M) were also investigated, showing a broad variance between 0.32 and 0.51 compared to the standard (quinine sulphate dissolved in 1 N sulfuric acid; $\Phi_{PL} = 0.546$) suggesting their good fluorescence properties, which not only reveal its unique molecular

dynamics but also point towards its significant potential in applications related to optoelectronics. The higher homologues in the series lead to a stronger emission and a higher fluorescence quantum yield. The displayed stokes shifts are nearly the same for all the compounds, ranging from 67 to 73 nm **(Table 2.3)**.

In conclusion, all of the synthesised compounds have photoluminescence spectra that show emission in the blue region = 400-470 nm, indicating that all of the materials have blue light emission properties that can be used in potential applications such as OLED materials, biotags for biological sensing applications, and fluorescent probes in biological applications [65–67].

Table 2.3: UV and fluorescence peaks for compounds **1a-m.**

Compounds	UV (nm)	Fluorescence(nm)	Stokes shift(nm)[a]	Φ_{PL}[b]
1a	266, 334	407, 433, 460	73	0.32
1b	269, 337	407, 432, 460	70	0.35
1c	269, 339	406, 431, 459	67	0.33
1d	262, 334	407, 431, 458	73	0.38
1e	270, 338	407, 433, 460	69	0.35
1f	269, 338	407, 432, 458	69	0.36
1g	269, 338	407, 431, 457	69	0.41
1h	269, 339	406, 431, 458	67	0.39
1i	269, 338	407, 431, 457	69	0.42
1j	269, 339	407, 431, 458	68	0.47
1k	269, 339	408, 433, 457	69	050
1l	269, 339	407, 432, 458	68	0.48
1m	269, 339	406, 431, 458	67	0.51

[a]Excited at 340 nm.

[b]Determined using quinine sulphate as standard (Φ_{PL} = 0.546 in 1N H_2SO_4).

2.3.5. Anti-oxidant activity

The in vitro antioxidant activity of all the mesogens was evaluated using a previously described technique [68]. The standard solution of mesogens at a conc. of 1 mg/mL was diluted to the final concentrations using DMSO. Absorbance was recorded at the λmax of 517 nm using a UV-Visible Spectrophotometer (Shimadzu UV-1800 spectrophotometer- Japan) [69]. The mesogens inhibition % against DPPH was determined according to reference [70].

"% Inhibition = $[(A_{control} - A_{sample}) / A_{control}] \times 100$"

where $A_{control}$ = abs. of control, A_{sample} = abs. of test compounds.

The radical scavenging activity is expressed as % of inhibition as well as an IC_{50} value. It was measured in comparison to the standard ascorbic acid.

Table 2.4: Antioxidant activity: % inhibition and IC_{50} values of the DPPH free radical scavenging

Sample code	% Inhibition[a]			IC_{50} (µg/ml)
	50 µg/ml	100µg/ml	200µg/ml	
1a	37.76±0.24	57.28±0.85	84.14±0.84	84.6
1b	38.80±0.31	58.16±0.96	83.98±0.12	81.7
1c	32.55±0.90	59.79±0.95	73.94±0.78	95.53
1d	31.61±0.29	61.85±0.68	80.51±0.97	90.55
1e	46.68±0.39	65.08±0.59	94.85±0.08	57.27
1f	35.11±0.34	56.93±0.61	82.19±0.19	90.19
1g	45.30±0.26	59.93±0.17	90.85±0.41	66.2
1h	24.99±0.04	51.78±0.19	81.23±0.87	109.34
1i	33.16±0.45	42.22±0.24	65.08±0.49	131.42
1j	28.33±0.08	58.78±0.63	75.48±0.62	102.35
1k	30.44±0.92	46.75±0.99	57.55±0.98	146.56
1l	25.49±0.18	51.20±0.92	58.36±0.25	141.79
1m	29.66±0.40	43.85±0.24	53.54±0.64	167.56
STD[b]	45.17±0.01	66.65±0.41	93.84±0.74	57.99
Control[c]	-	-	-	-

[a] Values represent the mean ± standard error mean (SEM) of three experiments.

[b] Ascorbic acid used as standard

[c] No inhibition

The results obtained in **Table 2.4** indicate that all the synthesised derivatives exhibited a comparable degree of scavenging activity against the DPPH radical, with the lowest scavenging activity at 200 µg/mL concentration was for **1m** with 53.54±0.64%. This compound also exhibited the weakest IC_{50} value of 167.56 µg/mL. The compounds **1a-g** shows the good to moderate scavenging activity with a comparably low IC_{50} value then **1h-m** (higher homologous) in the series. The compounds **1e** even displayed higher scavenging activity at the lowest concentration, with an IC_{50} value of 57.27 µg/mL as compared to the standard ascorbic

acid (57.99 µg/mL). It is interesting to note that the increase in the alkoxy chain length at the terminal position of the phenyl ring in the series tends to reduce the anti-oxidant activity.

In general, all the synthesized compounds exhibited good to moderate radical scavenging activity compared to the reference. Among the synthesized compounds, compounds **1e** and **1g** exhibited the best antioxidant activity, as shown in **Table 2.4**.

2.3.6. Effect of lateral methoxy substitution on phase transition

In order to study the effect of core lateral substitution on the mesomorphic properties, a new homologous series of compounds was synthesized similar to the above reported series. The core benzene ring was substituted by a lateral methoxy (-OCH_3) group. To synthesize these compounds, a scheme similar to **Scheme 2.1** was followed. To substitute the core, instead of p-hydroxybenzaldehyde, 4-hydroxy-3-methoxybenzaldehyde (Vanillin) was used. By following this, a new series of compound **1' a-m** was obtained, which has a lateral substitution as shown in **Figure 2.12** below. **Table 2.5** show transition temperature for the series **1' a-m.**

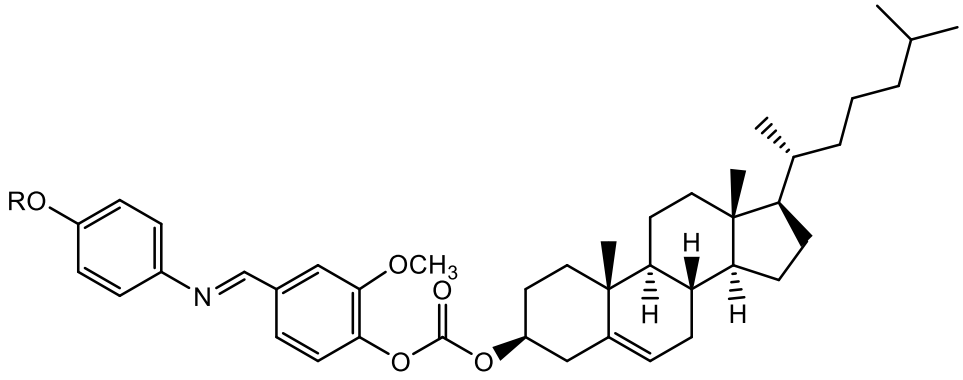

1' a-m

R = n-C_nH_{2n+1}, n = 1 to 8, 10, 12, 14, 16 and 18.

Figure 2.12: Molecular structure for laterally substituted compounds **1' a-m**

Typical lateral groups include halogens, methyl, methoxy, ethyl, ethoxy, nitro, cyano, and other small groups. Some unusual LC include large lateral groups, including aromatic rings. Each lateral substitution results in a broader molecule and a decrease in the "length-to-breadth ratio", X. According to "van der Waals molecular-statistical theories", this often lowers the clearing temperature. There is a (weak) correlation between X and T_{N-I} in compounds with lateral substitution. Correlations have been discovered between the size of the lateral groups as well as clearing temperatures [71]. Multiple studies in published literature demonstrate that smaller lateral groups have a lesser effect on lowering the clearing temperature compared to

larger ones [71–74]. Compounds require very lower temperatures of melting in order to be suitable for applications. Several instances in previous studies (e.g. [75]) demonstrate that the melting temperature (T_m) of a material, and therefore its clearing temperature, may be reduced by lateral substitution. The impact is likely caused by the decrease in the symmetry of molecular structure, since effect of lateral group seems to be reduced in less symmetric molecules. Lateral groups have a greater impact on the stability of smectic mesophase compared to the nematic. They are deliberately used to prevent the formation of the smectic phase in the development of liquid crystals for display purposes.

Table 2.5: Phase transition temperature of compounds **1'a-m** [a, b]

Sample code	No. of C	Heating Temp °C	Cooling Temp °C
1'a	1	Cr 189.9 N* 200.5 I	I 199.0 N* 78.4 Cr
1'b	2	Cr 213.6 I	I (211.2) N* 70.5 Cr
1'c	3	Cr 204.2 N* 216.2 I	I 214.80 N* 88.7 Cr
1'd	4	Cr 209.7 I	I (208.1) N* 68.4 Cr
1'e	5	Cr 198.1 N* 206.1 I	I 204.9 N* 77.9 Cr
1'f	6	Cr 195.9 N* 202.4 I	I 200.1 N* 82.6 Cr
1'g	7	Cr 196.8 N* 200.2 I	I 198.6 N* 72.3 Cr
1'h	8	Cr 196.2 N* 198.8 I	I 197.0 N* 80.2 Cr
1'i	10	Cr 181.8 SmA 191.2 I	I 190.4 SmA 90.6 Cr
1j'	12	Cr 168.9 SmA 183.7 I	I 182.1 SmA 98.3 Cr
1'k	14	Cr 158.8 SmA 176.5 I	I 175.7 SmA 101.8 Cr
1'l	16	Cr 149.9 SmA 172.8 I	I 170.9 SmA 98.6 Cr
1'm	18	Cr 149 SmA 170.4 I	I 169.1 SmA 88.4 Cr

Temperature in parenthesis ( ) indicates monotropic transition; Cr = crystal, SmA = smectic A phase, SmC* = chiral smectic C phase, N* = chiral nematic/ cholesteric phase, TGB_A = twist grain boundary A phase, I = isotropic temperature.

[a]Phase transition temperatures were determined/confirmed by both Polarising optical microscope (POM) and differential scanning calorimetry (DSC) studies: peak temperatures in the DSC thermograms obtained during the first heating and cooling cycles (scanning rate = 5°C min^{-1}) coupled with POM measured temperatures are given; [b]Transition temperatures of some of the

compounds were determined with the aid of a POM study as the expected well-resolved thermograms of both heating and cooling cycles could not be obtained.

Figures 2.13(a) and **(b)** displays the graphical representation of phase transition temperature and clearing temperatures of all the compounds of series **1a-m** and **1' a-m.** It is evident that due to the introduction of the lateral methoxy group in the core of the molecule a large difference is observed in the clearing points (~ 100°C) of the compounds in series **1' a-m.** Also, the derivatives **1' b** and **1' d** are non-mesogenic in nature. Additionally, the SmC* phase in **Series 1'a-m** diminished which was visible in **Series 1 a-m**.

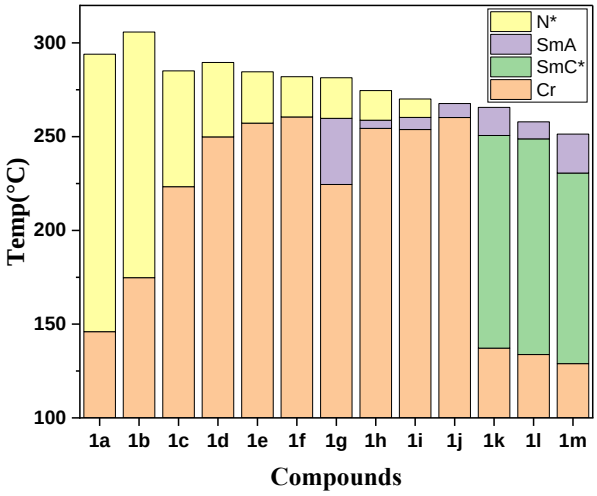

Figures 2.13 (a): Phase transition of **1a-m**

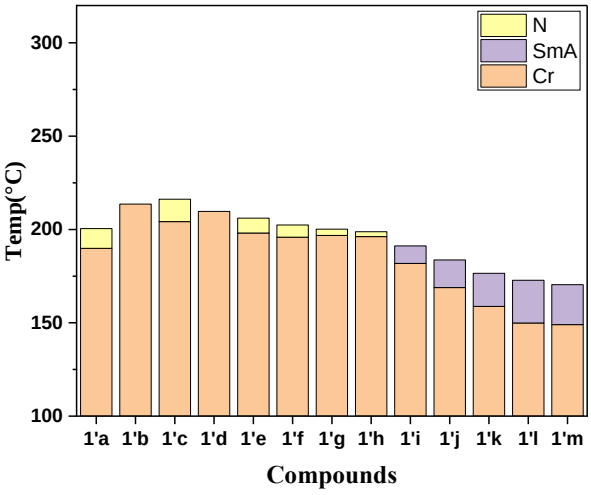

Figures 2.13 (b): Phase transition of **1'a-m**

From the available literature the reasons and effects of lateral substitution on phase can be ascertained as follows.

Substituents may push long molecular axes apart, diminishing intermolecular attraction and thereby decreasing liquid crystal thermal stability, leading to;

(i) Reduction in the temperature at which the mesophase emerges.

(ii) Decrease in the stability of the mesophase.

(iii) Abolish any smectogenic property irrespective of terminal group chain length.

2.3.7. DFT studies

2.3.7.1. Optimized Molecular Structures and HOMO-LUMO Energies

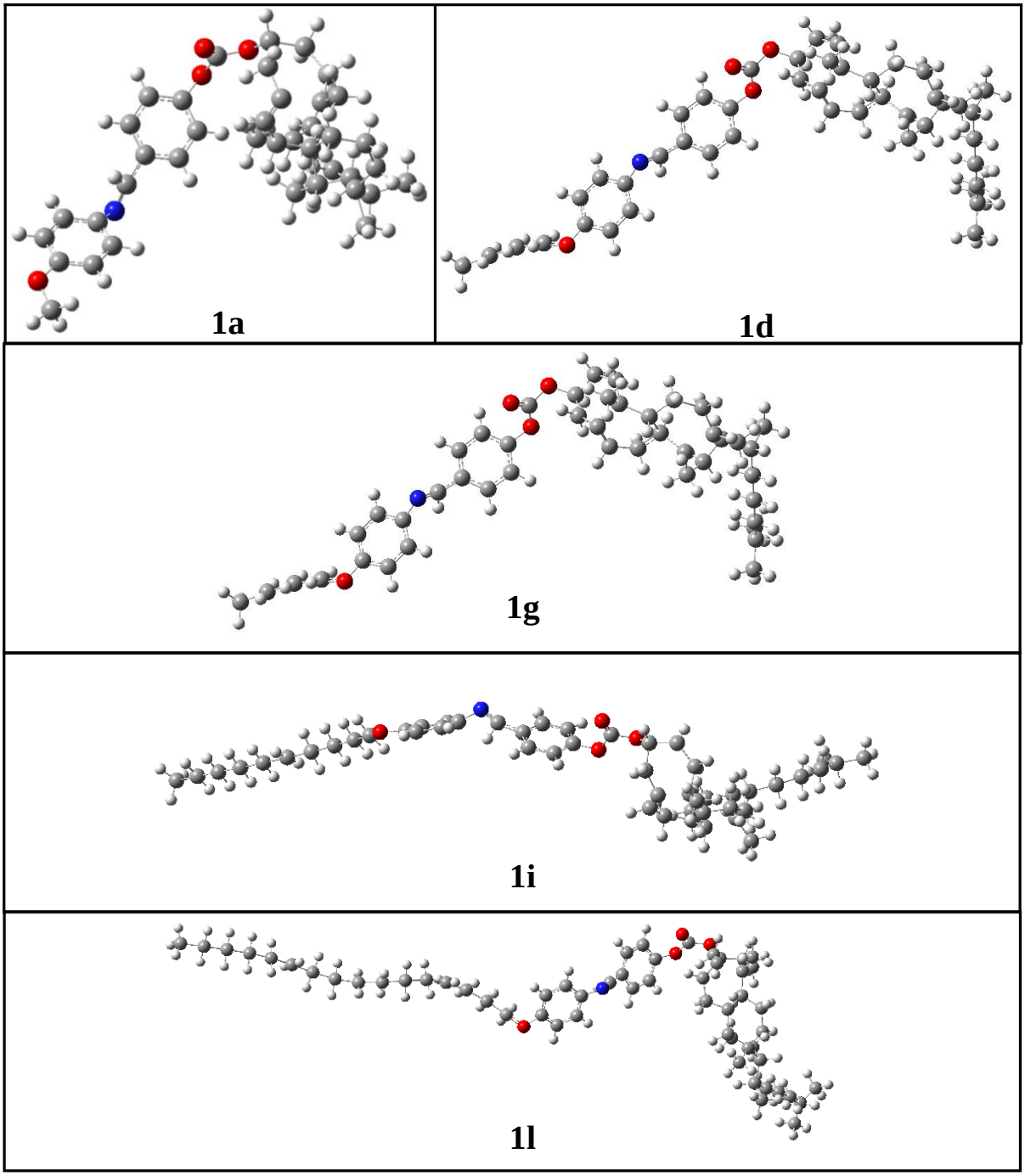

Figure 2.14: Optimized molecular structures of some cholesterol derivatives

The chemical quantum properties of the synthesized mesogens were determined through computational calculations using the DFT method. The geometrical structures were optimized using the B3LYP method in the gas phase, using the 6-31 G basis set with Gaussian

09, revision A.02 software [76]. The optimized structure of each component in the system showed stability by the absence of any imaginary frequencies, as seen in **Figure 2.14**.

Molecular structures were shown using grey, blue, red, and white colours to symbolize C, N, O, and H atoms, respectively. The atoms were linked together by sigma and pi bonds to generate a 3-D structure. **Figure 2.14** displays the most efficient molecular configurations for cholesterol derivatives, and **Table 2.6** shows the optimized energies of particular derivatives. **Figure 2.15** shows the graphical representation of relationship between the number of C in the terminal chain in cholesterol derivatives and the energy minima in Hartree units. The figure shows that as the number of carbons in the terminal chain increases, there is a drop in energy minima, suggesting a more stable molecular structure. The change is due to the increased flexibility as well as confirmational freedom in the higher homologues.

Molecular frontier orbitals provide crucial insights on the chemical reactivity of molecules. An elevated E_{HOMO} signifies enhanced electron-donating capacity, while a reduced E_{LUMO} implies less ability to accept electrons. According to Pearson's "Hard and Soft Acids and Bases" theory, molecules classified as soft have lower energy gap values ($\Delta E_{gap} = E_{LUMO} - E_{HOMO}$), making them more stable and reactive [77].

Table 2.6: Optimized energy (in hartree)

Sample	Energy Minima (Hartree)
1a	-1988.554
1d	-2105.849
1g	-2223.098
1i	-2340.596
1l	-2574.977

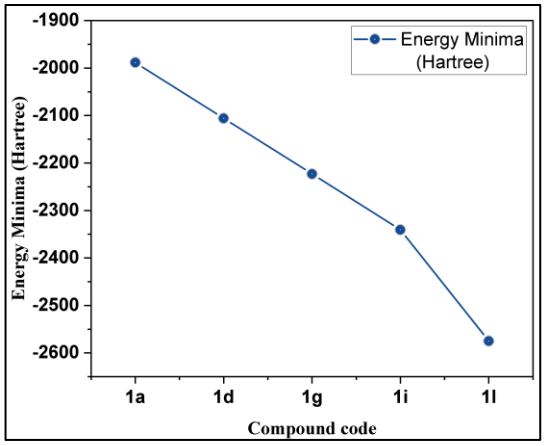

Figure 2.15: Dependence of the terminal alkoxy chain on the energy minima

Figure 2.16 (a-c) shows 3D iso surface plots of the HOMO and the LUMO of selected compounds, illustrating the composition of the respective atomic orbits. The figures visually illustrate the molecule's electron density distribution by highlighting areas with greater and lower electron densities. The majority of electron density in the HOMO in **1a** and **1d** was situated above the iso-octyl side chain of cholesterol moiety, while that of LUMO for **1a** was mainly on Schiff's base group and aromatic rings and for **1d** LUMO was mainly situated over the butoxy side chain. For derivatives **1g** and **1i** both HOMO and LUMO electron density lies

over the alkoxy side chains, while for compound **1l** in HOMO it lies mainly over the terminal methylene group and in LUMO it was focused mainly over the methylene group near ether linkage.

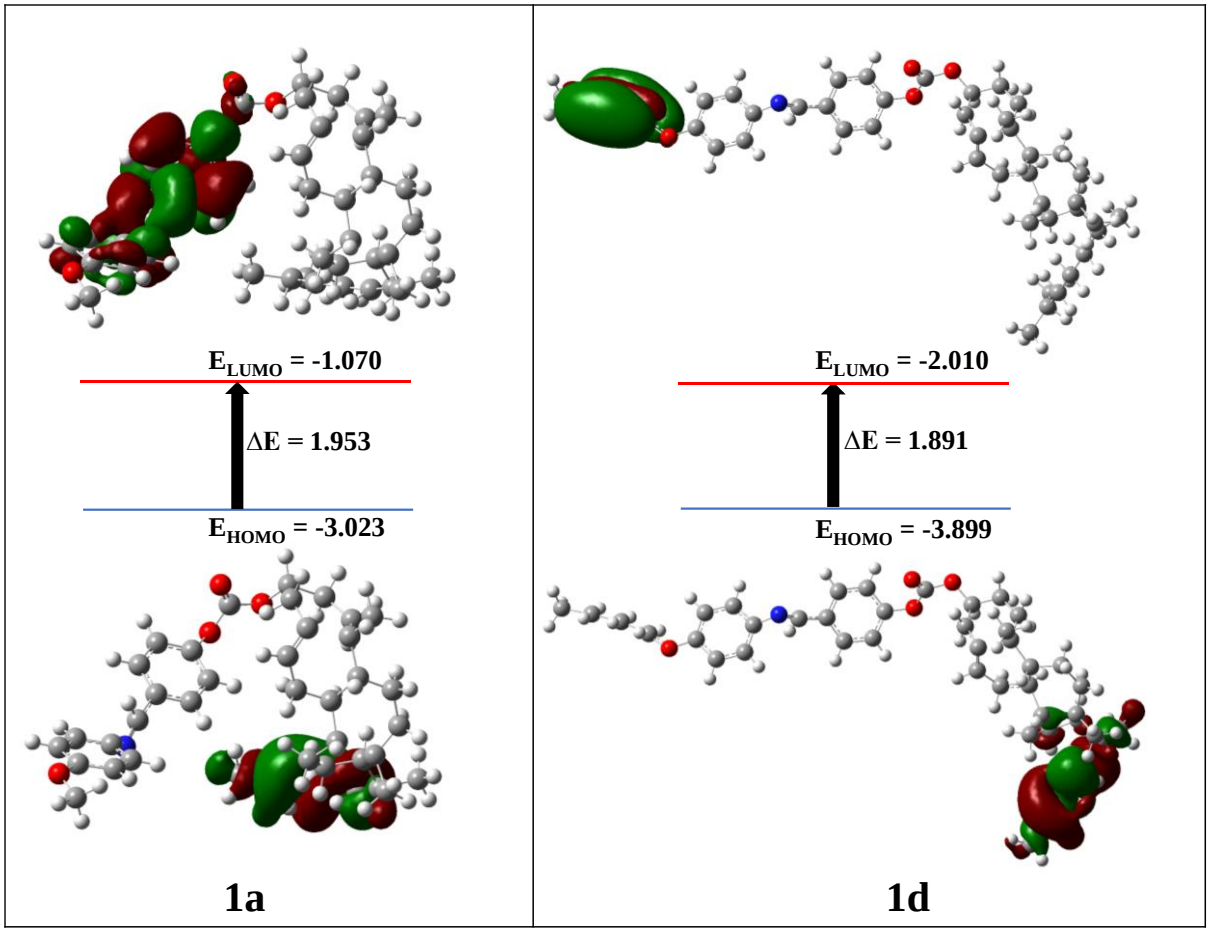

Figure 2.16 (a): FMO contours of structures **1a** and **1d**

It was noted that with the increasing terminal chain length the energy gap (ΔE) tends to decrease. This can be used to explain the photoluminescence intensity as well the quantum yields in PL spectra. A lower ΔE usually suggests a greater probability of electronic transitions, electrical conductivity, and involvement in chemical processes, leading to increased fluorescence [78]. This is because excited electrons relax more efficiently to the ground state owing to the smaller gap, resulting in a greater amount of light emission. The data in the **Table 2.7** shows that the values of ΔE decreases in the order: **1a** > **1d** > **1g** > **1i** > **1l** while the PL intensity and quantum yield increases inversely, in the order **1a** < **1d** < **1g** < **1i** < **1l** (**Table 2.3** and **Figure 2.11**). Also, from **Table 2.7** calculations it was determined that the reactivity of the mesogens reduced in the order: **1a** < **1d** < **1g** < **1i** < **1l**, respectively.

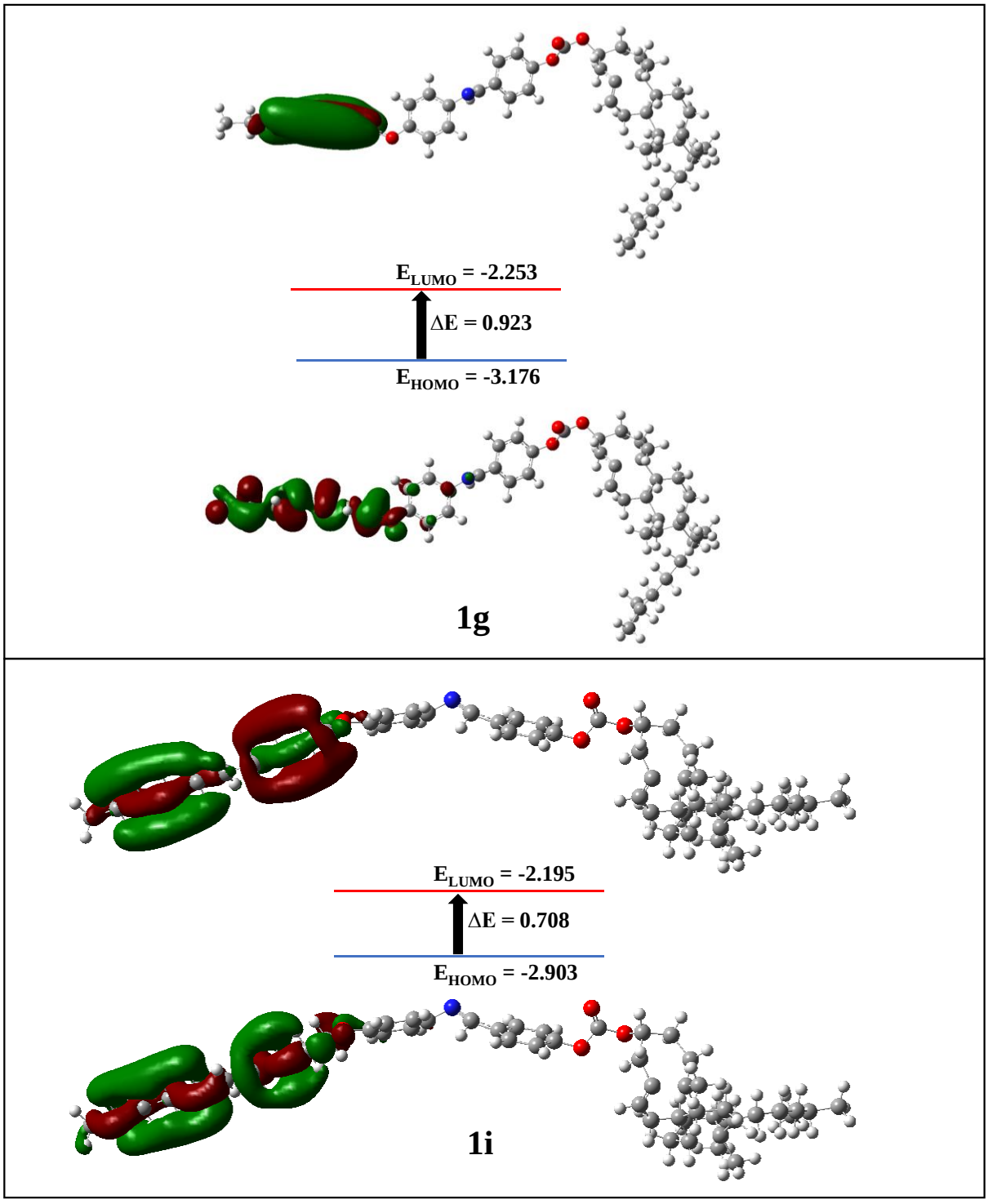

Figure 2.16 (b): FMO contours of structures **1g** and **1i**

Table 2.7 displays the frontier MO energy along with chemical reactivity aspects for the optimized structure of molecules [79]. The electronic chemical potential (μel), chemical hardness (η), and electrophilicity index (ω) are reactivity descriptors that provide important information on the chemical reactivity and stability of compounds. The compounds had chemical potentials ranging from -2.04 to -2.95 eV and hardness values ranging from 0.12 to 0.98 eV, with the lowest found for **1l**. Compound **1l** is determined to be softer and more reactive

than the other compounds in the series. A rising tendency in electrophilicity is found in the order: **1a** < **1d** < **1g** < **1i** < **1l**, indicating a drop in electron density or a raise in electron-withdrawing property in the mesogens. This makes **1l** more reactive towards electrophiles.

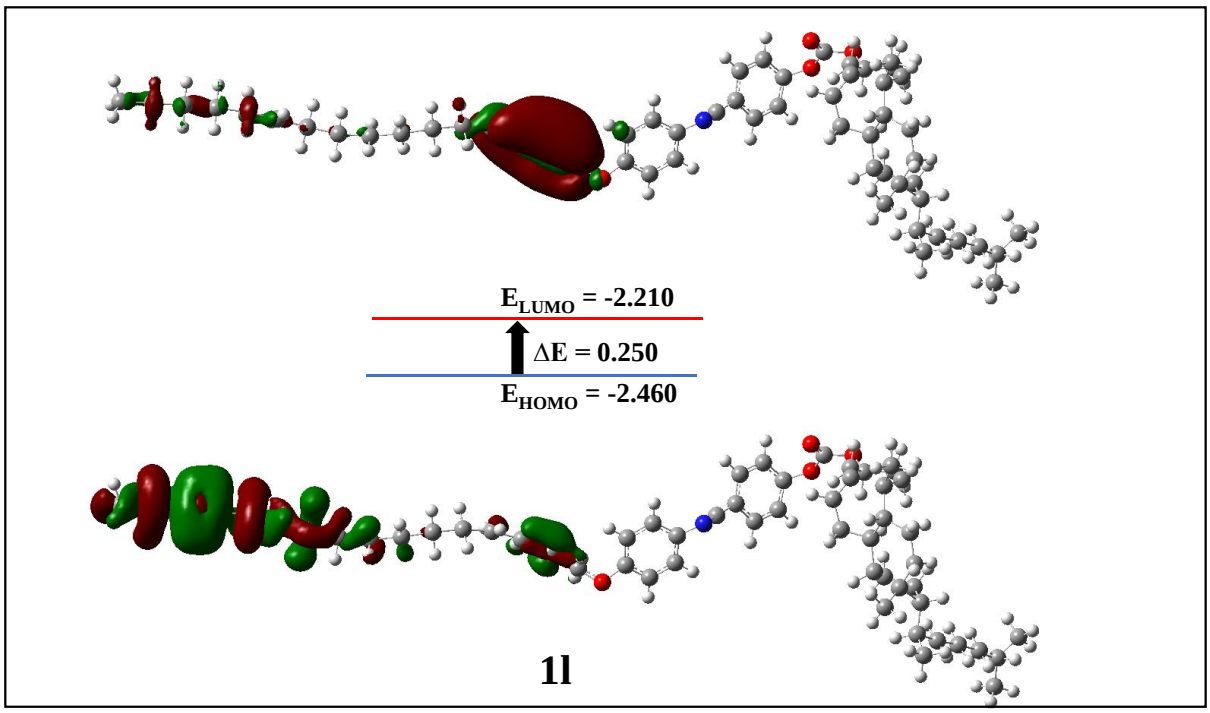

Figure 2.16 (c): FMO contours of structure **1l**

Table 2.7. Calculated molecular properties of the cholesterol compounds using DFT

Sample	E_{HOMO} (eV)	E_{LUMO} (eV)	ΔE (eV)	η Global hardness	δ = 1/η Global softness	μ_{el} (eV)	ω Electrophilicity index
1a	-3.023	-1.070	1.953	0.98	1.02	-2.04	2.14
1d	-3.899	-2.010	1.891	0.94	1.05	-2.95	4.62
1g	-3.176	-2.253	0.923	0.46	2.16	-2.71	7.98
1i	-2.903	-2.195	0.708	0.35	2.82	-2.54	9.18
1l	-2.460	-2.210	0.250	0.12	7.99	-2.33	21.81

Dipole moments have been calculated for the selected compounds in three Cartesian axis **(Table 2.8)**. The dipole moments of these compounds are significantly greater than the dipole moment of cholesterol previously reported [80].The high dipole moments points towards mesogenic properties of the compounds. Among the derivatives analyzed, compound

1a exhibits the smallest charge separation with a dipole moment of 4.5990 debye, while compound **1i** has the highest dipole moment of 5.3724 debye.

Table 2.8: Dipole moment for cholesterol derivatives

Sample	μ_x	μ_y	μ_z	Dipole Moment μ_{dip} (Debye)
1a	0.4822	-1.3612	-4.3664	4.5990
1d	0.7902	4.8838	1.3541	5.1293
1g	-3.2043	3.8741	1.7329	5.3178
1i	2.0234	3.6670	3.3648	5.3724
1l	4.3003	2.0615	-0.1716	4.7720

2.3.7.2. Molecular Electrostatic Potential (MEP)

The charge distribution map for the mesogens was estimated using the same approach and basis sets as the electrostatic potential (MEP) **(Figure 2.17)**. The negatively charged atomic sites illustrated in the red region were found to be concentrated on the carbonate, azomethine and ether linkages. The atomic locations with the lowest negative charge illustrated in the blue region were identified on the iso-octyl side chain of cholesterol and the alkyl side chain. The distribution mapping of the charges might illustrate the emergence of the observed mesophase of the liquid crystals. The improvement of the smectic mesophase across all studied compounds may be due to the existence of extended terminal chains. According to the ESP charge distribution mapping, the compound's elongated chains make it more polarizable, which increases the total intermolecular attraction at the terminals and enhances the smectic mesophase.

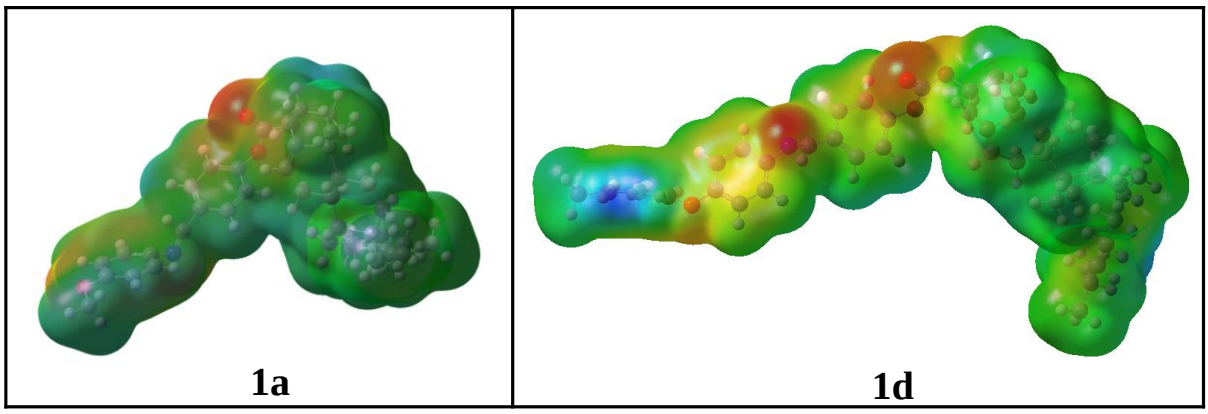

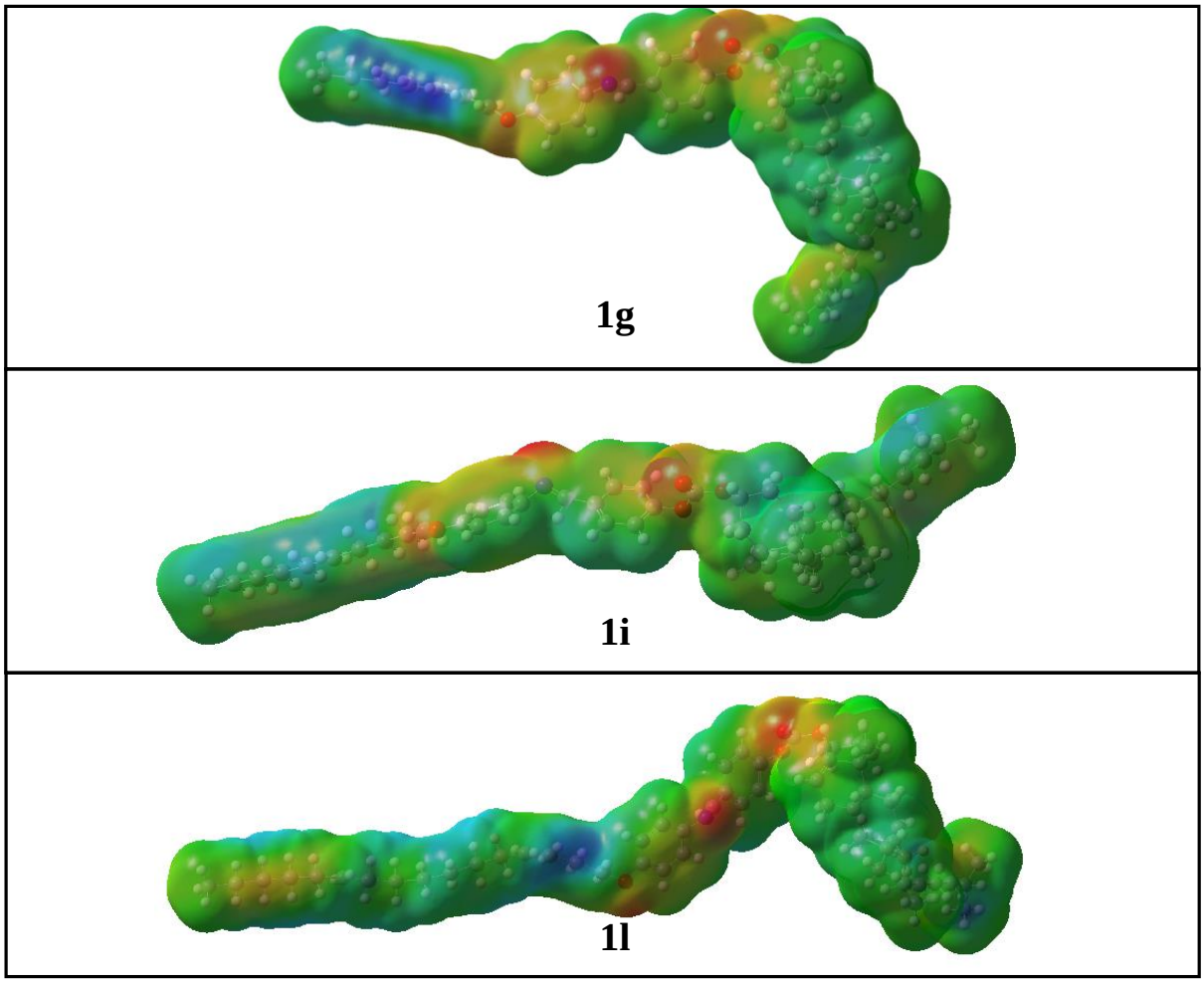

Figure 2.17: Molecular electrostatic potentials (MEP) for selected mesogens

2.4. Conclusion

In conclusion, we have synthesised twenty-six new mesogenic Schiff's base derivatives (**1a-m and 1' a-m)** by condensing 4-n-alkoxy aniline with 4-formyl phenyl cholesteryl carbonate and 4-formyl 3-methoxy phenyl cholesteryl carbonate. All the final derivatives **1a-m** show mesomorphic properties. The methyl to n-hexyl derivatives show an enantiotropic chiral nematic mesophase except for the n-pentyl and n-hexyl derivatives, which also exhibit an additional TGB_A-SmA monotropic mesophase on cooling. The n-heptyl to n-decyl homlogues show enantiotropic TGB_A-SmA and N* phase transitions. The n-dodecyl derivative shows only the enantiotropic SmA phase, while the n-tetradecyl to n-octadecyl show the enantiotropic SmA and SmC* mesophases. In the plot of transition temperature versus number of carbon atoms in the alkoxy chain, the smectic A to chiral nematic curve rises to maximum, while the Smectic C* to Smectic A shows a sinking inclination. The cholesteric/SmA/SmC*-

isotropic curve shows the usual falling tendency. All the compounds are UV-active and show photoluminescence in the blue emission region. With increasing terminal chain length, stronger emission and the higher fluorescence quantum yield was observed. All the compounds show moderate to good anti-oxidant activity. The effect of lateral methoxy substitution was also examined **(1' a-m)** and results indicate that the lateral substitution caused a drastic reduction in thermal stability of LC, mesophase stability as well as disappearance of some smectogenic nature of the mesogens. DFT calculations were carried out to give insights on theoretical chemical reactivity studies, considering the Frontier MOs and MEP mapping, measuring the energy gaps and giving areas of low and high electron density. The investigation of their application aspects would be quite fascinating.

2.5. References

[1] Jones DW. Soap, Science and Flat-Screen TVs: A History of Liquid Crystals, by David Dunmur and Tim Sluckin. Contemporary Physics. 2011;**52**:613–614.

[2] Yelamaggad CV, Shanker G, Hiremath US, et al. Cholesterol-based nonsymmetric liquid crystal dimers: an overview. J Mater Chem. 2008;**18**:2927–2949.

[3] Bobrovsky AYu, Boiko NI, Shibaev VP, et al. New Chiral Nematic Materials with Photovariable Helical Supramolecular Structure for Reversible Optical Data Recording. Advanced Materials. 2000;**12**:1180–1183.

[4] Palffy-Muhoray P. Liquid crystals New designs in cholesteric colour. Nature. 1998;**391**:745–746.

[5] Zhan X, Jing X, Wu C. Synthesis and mesomorphic properties of a novel series of cholesterol-based liquid crystalline tetramers. Liquid Crystals. 2009;**36**:1349–1354.

[6] Kurihara S, Nomiyama S, Nonaka T. Photochemical Control of the Macrostructure of Cholesteric Liquid Crystals by Means of Photoisomerization of Chiral Azobenzene Molecules. Chem Mater. 2001;**13**:1992–1997.

[7] Urata K, Takaishi N. Cholesteryl ester compounds containing alkyl branched acyl groups — their preparations, properties and applications. Lipid / Fett. 1997;**99**:327–332.

[8] Thiemann T, Vill V. Homologous Series of Liquid Crystalline Steroidal Lipids. Journal of Physical and Chemical Reference Data. 1997;**26**:291–333.

[9] Goodby JW, Waugh MA, Stein SM, et al. Characterization of a new helical smectic liquid crystal. Nature. 1989;**337**:449–452.

[10] Hu D, Qian Z. Chapter 30 - Cholesterol in drug delivery systems. In: Bukiya AN, Dopico AM, editors. Cholesterol [Internet]. Academic Press; 2022 [cited 2023 Jun 12]. p. 797–824. Available from: https://www.sciencedirect.com/science/article/pii/B9780323858571000080.

[11] E Silva ATM, Maia ALC, de Oliveira Silva J, et al. Synthesis of cholesterol-based neoglycoconjugates and their use in the preparation of liposomes for active liver targeting. Carbohydrate Research. 2018;**465**:52–57.

[12] Lin Y-K, Fang J-Y, Wang S-W, et al. Synthesis and characterization of triple-responsive PNiPAAm-S-S-P(αN3CL-g-alkyne) copolymers bearing cholesterol and fluorescence monitor. Reactive and Functional Polymers. 2018;**130**:29–42.

[13] Asayama S, Nagashima K, Negishi Y, et al. Byproduct-Free Intact Modification of Insulin by Cholesterol End-Modified Poly(ethylene glycol) for in Vivo Protein Delivery. Bioconjugate Chem. 2018;**29**:67–73.

[14] Bernhard Y, Gigot E, Goncalves V, et al. Direct subphthalocyanine conjugation to bombesin vs. indirect conjugation to its lipidic nanocarrier. Org Biomol Chem. 2016;**14**:4511–4518.

[15] Palakollu V, Kanvah S. Cholesterol-tethered AIEE fluorogens: formation of self-assembled nanostructures. RSC Adv. 2015;**5**:33049–33057.

[16] Ikejiri M, Mori K, Miyagi R, et al. A hybrid molecule of a GFP chromophore analogue and cholestene as a viscosity-dependent and cholesterol-responsive fluorescent sensor. Org Biomol Chem. 2017;**15**:6948–6958.

[17] Gupta M, Pal V, Pal SK. Photo-responsive liquid crystals derived from azobenzene centered cholesterol-based tetramers. New J Chem. 2018;**42**:8765–8772.

[18] Chen S, Hong B, Guo H, et al. The mesomorphic and photophysical properties of perylene liquid crystals with different bay-rigid spacers. Liquid Crystals. 2018;**45**:793–800.

[19] Ooi Y-H, Yeap G-Y. λ-Shaped liquid crystal trimers with dual terminal cholesteryl moieties: synthesis and concomitant of N*, SmA and cholesteric glassy phases. Liquid Crystals. 2018;**45**:204–218.

[20] Draper ER, Adams DJ. Low-Molecular-Weight Gels: The State of the Art. Chem. 2017;**3**:390–410.

[21] Tan X, Li Z, Xia M, et al. Reversible photoresponsive chiral liquid crystal and multistimuli responsive organogels based on a cholesterol-azobenzene dimesogen. RSC Adv. 2016;**6**:20021–20026.

[22] Bu M, Cao T, Li H, et al. Synthesis and biological evaluation of novel steroidal 5α,8α-endoperoxide derivatives with aliphatic side-chain as potential anticancer agents. Steroids. 2017;**124**:46–53.

[23] Huang Y, Wen H, Zheng J, et al. Synthesis, characterization, and biological evaluations of some steryl 2-methoxybenzoates as anticancer agents. Natural Product Research. 2019;**33**:1101–1105.

[24] Aly MRES, Saad HA, Mohamed MAM. Click reaction based synthesis, antimicrobial, and cytotoxic activities of new 1,2,3-triazoles. Bioorganic & Medicinal Chemistry Letters. 2015;**25**:2824–2830.

[25] Ansari A, Ali A, Asif M, et al. Facile one-pot multicomponent synthesis and molecular docking studies of steroidal oxazole/thiazole derivatives with effective antimicrobial, antibiofilm and hemolytic properties. Steroids. 2018;**134**:22–36.

[26] Elkihel L, Bourass J, Dherbomez M, et al. Synthesis of Aminocholesterol Derivatives with Antibiotic Properties. Synthetic Communications. 1997;**27**:1951–1962.

[27] Begum A, Borah P, Chowdhury P. Microwave (MW) promoted high yield expedient synthesis of steryl ferulates – A class of novel biologically active compounds: A comparative study of their antioxidant activity with that of naturally occurring γ-oryzanol. Steroids. 2016;**107**:37–44.

[28] Sarkar A, Das J, Ghosh P. p-TsOH-Catalyzed one-pot transformation of di- and trihydroxy steroids towards diverse A/B-ring oxo-functionalization. New J Chem. 2017;**41**:9051–9060.

[29] Weiss S, Neu PM, Ludwig C, et al. Novel Method for the Synthesis of Cholesteryl Glucosides starting from Disaccharides. European Journal of Lipid Science and Technology. 2018;**120**:1700389.

[30] Yelamaggad CV, Nagamani SA, Hiremath US, et al. Cholesterol-based dimeric liquid crystals: synthesis and mesomorphic behaviour. Liq Cryst. 2001;**28**:1009–1015.

[31] Galatina AI, Novikova NS, Derkach LG, et al. Structure and Mesomorphism of Cholesteric Liquid Crystals. Molecular Crystals and Liquid Crystals. 1986;**140**:11–81.

[32] Harwood SM, Toyne KJ, Goodby JW, et al. The synthesis of cholest-5-ene-3beta-carboxylates and a comparison of their mesomorphic behaviour with isomeric cholesterol esters with a reversed ester linkage. Liquid Crystals. 2000;**27**:443–449.

[33] Shubashree S, Sadashiva BK. Twist grain boundary smectic A phase in compounds derived from cholesterol. Current Science. 2003;**85**:1061–1065.

[34] Shubashree S, Sadashiva BK. Synthesis and mesomorphic properties of compounds exhibiting the undulated twist grain boundary smectic C* phase. Liquid Crystals. 2004;**31**:81–89.

[35] Davis P, Cholaphanes A. et al.; steroids as structural components in molecular engineering. Chemical Society Reviews. 1993;**22**:243–253.

[36] Fang Z, Wu C. Investigation on thermal behaviour and optical properties of non-symmetric cholesterol-based twin liquid crystals with thioester linkages. Liquid Crystals. 2020;**47**:1086–1099.

[37] Lee J, Jin J, Achard MF, et al. Cholesterol-based hydrogen-bonded liquid crystals. Liquid Crystals. 2003;**30**:1193–1199.

[38] Yeap G-Y, Alshargabi A, Mahmood WAK, et al. Synthesis, characterization and molecular organization for induced smectic phase of triazole ring in non-symmetric liquid crystalline dimer. Tetrahedron. 2015;**71**:3939–3945.

[39] Korkmaz B, Kırsoy A, Okutan M, et al. Synthesis and investigation of new cholesteryl carbamate-based liquid crystals. J Mater Sci: Mater Electron. 2022;**33**:12224–12238.

[40] Lee H-C, Lu Z, Henderson PA, et al. Cholesteryl-based liquid crystal dimers containing a sulfur–sulfur link in the flexible spacer. Liq Cryst. 2012;**39**:259–268.

[41] Chan T-N, Lu Z, Yam W-S, et al. Non-symmetric liquid crystal dimers containing an isoflavone moiety. Liquid Crystals. 2012;**39**:393–402.

[42] Donaldson T, Staesche H, Lu ZB, et al. Symmetric and non-symmetric chiral liquid crystal dimers. Liquid Crystals. 2010;**37**:1097–1110.

[43] Hiremath US. Synthesis and characterization of novel chiral dimers exhibiting highly frustrated liquid crystal phases. Tetrahedron. 2014;**70**:4745–4753.

[44] Donaldson T, Henderson PA, Achard MF, et al. Non-symmetric chiral liquid crystal trimers. Liquid Crystals. 2011;**38**:1331–1339.

[45] Donaldson T, Henderson PA, Achard MF, et al. Chiral liquid crystal tetramers. J Mater Chem. 2011;**21**:10935–10941.

[46] Hamley IW, Castelletto V, Parras P, et al. Ordering on multiple lengthscales in a series of side group liquid crystal block copolymers containing a cholesteryl-based mesogen. Soft Matter. 2005;**1**:355–363.

[47] Criswell TR, Klanderman BH, Batesky DC. Alkyl Carbonato Terminally Substituted Anils. Molecular Crystals and Liquid Crystals. 1973;**22**:211–238.

[48] Dierking I, Gießelmann F, Zugenmaier P, et al. Investigations of the structure of a cholesteric phase with a temperature induced helix inversion and of the succeeding Sc* phase in thin liquid crystal cells. Liquid Crystals. 1993;**13**:45–55.

[49] Dierking I, Gießelmann F, Zugenmaier P. TGB A∗ state in a homologous series of diarylethane α-chloroester ferroelectric liquid crystals. Liquid Crystals. 1994;**17**:17–22.

[50] Seshadri T. Novel ferrocene-based chiral Schiff's base derivative with a twist-grain boundary phase (TGBA) and a blue phase. Chem Commun. 1998;735–736.

[51] Dhar R. Twisted-grain-boundary (TGB) phases: nanostructured liquid-crystal analogue of Abrikosov vortex lattices. Phase Transitions. 2006;**79**:175–199.

[52] Bhat S V, Raghunathan VA, Kumar S. Synthesis and mesomorphic characterization of some novel steroidal mesogens: A structure–property correlation. J Mol Liq. 2021;**340**:117219.

[53] Majumdar KC, Ghosh T, Rao DSS, et al. Unsymmetrical cholesterol and benzoxazole-based liquid crystalline dimers: synthesis and characterisation. Liquid Crystals. 2011;**38**:1269–1277.

[54] Dierking I. The SmC* Subphases. Textures of Liquid Crystals [Internet]. John Wiley & Sons, Ltd; 2003. p. 123–134. Available from: https://onlinelibrary.wiley.com/doi/abs/10.1002/3527602054.ch8.

[55] Imrie CT. Laterally substituted dimeric liquid crystals. Liquid Crystals. 1989;**6**:391–396.

[56] Imrie CT, Taylor L. The preparation and properties of low molar mass liquid crystals possessing lateral alkyl chains. Liquid Crystals. 1989;**6**:1–10.

[57] Date RW, Imrie CT, Luckhurst GR, et al. Smectogenic dimeric liquid crystals. The preparation and properties of the α,ω-bis(4- *n* -alkylanilinebenzylidine-4′-oxy)alkanes. Liquid Crystals. 1992;**12**:203–238.

[58] Dave JS, Kurian G. Mesomorphic Behaviour of Cholesteryl Esters: IV: p-n-Alkoxybenzylidene-p'-Aminobenzoates of Cholesterolt. Molecular Crystals and Liquid Crystals. 1973;**24**:347–355.

[59] Tandel RC, Vora RA. Mesogenic amido ester with cholesteryl moiety. Phase Transitions. 2008;**81**:421–429.

[60] Karipcin F, Kabalcilar E, Ilican S, et al. Synthesized some 4-(2-thiazolylazo)resorcinol complexes: Characterization, thermal and optical properties. Spectrochimica Acta Part A: Molecular and Biomolecular Spectroscopy. 2009;**73**:174–180.

[61] Sharma BP, Subin JA, Marasini BP, et al. Triazole based Schiff bases and their oxovanadium(IV) complexes: Synthesis, characterization, antibacterial assay, and computational assessments. Heliyon. 2023;**9**:e15239.

[62] Fang Z, Cao C. Effect of molecular conformation on spectroscopic properties of symmetrical Schiff bases derived from 1,4-phenylenediamine. Journal of Molecular Structure. 2013;**1036**:447–451.

[63] Pathak G, Hegde G, Prasad V. Octadecylamine-capped CdSe/ZnS quantum dot dispersed cholesteric liquid crystal for potential display application: Investigation on photoluminescence and UV absorbance. Liquid Crystals. 2021;**48**:579–587.

[64] Kulkarni C, George SJ. Carbonate Linkage Bearing Naphthalenediimides: Self-Assembly and Photophysical Properties. Chemistry – A European Journal. 2014;**20**:4537–4541.

[65] Jebapriya JC, Jonathan DR, Kirupavathy SS, et al. Growth and characterization of a cyclohexanone based chalcone crystal 2(E)-(4-N,N-dimethylaminobenzylidene)-5-methylcyclohexanone for nonlinear optical applications. Optical Materials. 2020;**107**:110035.

[66] Lin L, Rong M, Luo F, et al. Luminescent graphene quantum dots as new fluorescent materials for environmental and biological applications. TrAC Trends in Analytical Chemistry. 2014;**54**:83–102.

[67] Bonifácio VDB, Correia VG, Pinho MG, et al. Blue emission of carbamic acid oligooxazoline biotags. Materials Letters. 2012;**81**:205–208.

[68] Paduch R, Wozniak A. The Effect of Lamium album Extract on Cultivated Human Corneal Epithelial Cells (10.014 pRSV-T). Journal of Ophthalmic and Vision Research. 2015;**10**:229.

[69] Mukhia R, Basistha B, Chhetri DR. Variation in Antioxidant Activity of a Rattan Species, Plectocomia himalayana Griff. by DPPH assay based on two different methods of Methanol Extraction. Research Journal of Pharmacognosy and Phytochemistry. 2018;**10**:175–178.

[70] Sahu R, Kar MK, Routray R. DPPH Free radical scavenging activity of some leafy vegetables used by tribals of Odisha. India. J Med Plants Stud. 2013;**1**:21–27.

[71] Gray GW. The Influence of Molecular Structure on Liquid Crystalline Properies. Molecular Crystals. 1966;**1**:333–349.

[72] Demus D, Hauser A. Selected topics in liquid crystal research [Internet]. (Ed.: H.-D. Koswig. Berlin: Akademie-Verlag; 1990. Available from: https://scholar.google.com/scholar_lookup?&title=Selected%20topics%20in%20liquid%20crystal%20research&pages=19-19&publication_year=1990&author=Demus%2CD&author=Hauser%2CA.

[73] Gray GW. Molecular Geometry and the Properties of Nonamphiphilic Liquid Crystals. Advances in Liquid Crystals [Internet]. Elsevier; 1976. p. 1–72. Available from: https://linkinghub.elsevier.com/retrieve/pii/B9780120250028500087.

[74] Leadbetter AJ. The molecular physics of liquid crystals [Internet]. (Eds.: G. W. Gray, G. R. Luckhurst),. London: Academic Press; 1979. Available from: https://scholar.google.com/scholar_lookup?&title=Molecular%20physics%20of%20liquid%20crystals&publication_year=1979&author=Leadbetter%2CA.J.

[75] Hird M, Toyne KJ, Gray GW, et al. The relationship between molecular structure and mesomorphic properties of 2,2′- and 3,2′-difluoroterphenyls synthesized by palladium-catalysed cross-couplings. Liquid Crystals. 1995;**1**8:1–11.

[76] Frisch M, Trucks G, Schlegel H, et al. Gaussian 09 (Revision A02). Gaussian Inc Wallingford CT. 2009;

[77] Pearson RG. Hard and Soft Acids and Bases. J Am Chem Soc. 1963;**85**:3533–3539.

[78] Bhattacharyya K. Single-molecule spectroscopy: Every molecule is different! Reson. 2015;**20**:151–164.

[79] Pearson RG. Chemical hardness and the electronic chemical potential. Inorganica Chimica Acta. 1992;**198–200**:781–786.

[80] Sarkar DD, Deb R, Chakraborty N, et al. Cholesterol-based dimeric liquid crystals: synthesis, mesomorphic behaviour of frustrated phases and DFT study. Liquid Crystals. 2013;**40**:468–481.